PHYSICAL REVIEW D **82,** 084031 (2010)

Relativistic magnetohydrodynamics in dynamical spacetimes: A new adaptive mesh refinement implementation

Zachariah B. Etienne, Yuk Tung Liu, and Stuart L. Shapiro[1]

Department of Physics, University of Illinois at Urbana-Champaign, Urbana, Illinois 61801, USA

(Received 8 July 2010; published 19 October 2010)

We have written and tested a new general relativistic magnetohydrodynamics code, capable of evolving magnetohydrodynamics (MHD) fluids in dynamical spacetimes with adaptive-mesh refinement (AMR). Our code solves the Einstein-Maxwell-MHD system of coupled equations in full $3+1$ dimensions, evolving the metric via the Baumgarte-Shapiro Shibata-Nakamura formalism and the MHD and magnetic induction equations via a conservative, high-resolution shock-capturing scheme. The induction equations are recast as an evolution equation for the magnetic vector potential, which exists on a grid that is staggered with respect to the hydrodynamic and metric variables. The divergenceless constraint $\nabla \cdot \boldsymbol{B} = 0$ is enforced by the curl of the vector potential. Our MHD scheme is fully compatible with AMR, so that fluids at AMR refinement boundaries maintain $\nabla \cdot \boldsymbol{B} = 0$. In simulations with uniform grid spacing, our MHD scheme is numerically equivalent to a commonly used, staggered-mesh constrained-transport scheme. We present code validation test results, both in Minkowski and curved spacetimes. They include magnetized shocks, nonlinear Alfvén waves, cylindrical explosions, cylindrical rotating disks, magnetized Bondi tests, and the collapse of a magnetized rotating star. Some of the more stringent tests involve black holes. We find good agreement between analytic and numerical solutions in these tests, and achieve convergence at the expected order.

DOI: 10.1103/PhysRevD.82.084031 PACS numbers: 04.25.D−, 04.40.Nr, 47.75.+f, 95.30.Qd

I. INTRODUCTION

Magnetized fluids in dynamical, strongly curved spacetimes play a central role in many systems of current interest in relativistic astrophysics. Such fluids may generate gamma-rays in gamma-ray bursts (GRBs), destroy differential rotation in nascent neutron stars arising from stellar core collapse or binary neutron star merger, form jets and influence disk dynamics around black holes, affect magnetorotational collapse of massive stars, etc. Many of these systems are promising sources of gravitational radiation for detection by laser interferometers such as LIGO, VIRGO, TAMA, GEO and LISA. Some also emit electromagnetic radiation, such as gamma-ray bursts, magnetized disks around black holes in active galactic nuclei (AGNs) and quasars, and binary supermassive black holes coalescing in ambient magnetized plasma. Accurate, self-consistent modeling of these systems requires a computational scheme capable of simultaneously accounting for magnetic fields, relativistic magnetohydrodynamics (MHD) and relativistic gravitation.

Over the past several years, we have developed a robust numerical scheme in $3+1$ dimensions that evolves the Einstein equations of general relativity for the gravitational field (metric), coupled to the equations of relativistic MHD for the matter and Maxwell's equations for a magnetic field [1]. Our approach is based on the BSSN (Baumgarte-Shapiro-Shibata-Nakamura) formalism to evolve the metric [2,3], a high-resolution, shock-capturing (HRSC) scheme to handle the fluids, and a constrained-transport scheme to treat magnetic induction [4]. This GRMHD code has been subjected to a rigorous suite of numerical tests to check and calibrate its validity [1]. The code has been applied to explore a number of important dynamical scenarios in relativistic astrophysics, including the collapse of magnetized, differentially-rotating hypermassive neutron stars to black holes [5–7], the collapse of rotating stellar cores to neutron stars [8], the collapse of rotating, supermassive stars and massive Population III stars to black holes [9], magnetized binary neutron star merger [10], binary black-hole-neutron stars [11,12], and the merger of binary black holes in gaseous environments [13]. The purpose of this paper is to present a generalization of our current GRMHD scheme that is compatible with adaptive mesh refinement (AMR).

Many problems in relativistic astrophysics require numerical simulations covering a large range of lengthscales. For example, to follow the final merger of a compact binary system with a total mass M, a lengthscale of $\sim M/30$ needs to be resolved to treat the strong-field, near-zone regions reliably. On the other hand, accurate gravitational wave calculations at lengthscale $\sim M$ must be performed far in the weak-field wave-zone at radius $r \gtrsim 100M$. AMR allows for sufficient resolution to be supplied to areas of the computational domain as needed, thus enabling us to resolve strong- and weak-field domains efficiently.

One of the most subtle issues in evolving the MHD equations is the preservation of the divergenceless constraint ($\nabla \cdot \boldsymbol{B} = 0$) during the evolution. When evolving

[*]Also at Department of Astronomy and NCSA, University of Illinois at Urbana-Champaign, Urbana, IL 61801, USA

the induction equations, numerical truncation error leads to violations of the divergenceless constraint, resulting in unphysical plasma transport orthogonal to the magnetic field, as well as violations of energy and momentum conservation (see e.g., [4,14,15]). In simulations using a uniformly spaced grid, ''constrained-transport'' schemes (see e.g., [4,16]) are commonly used to maintain the divergenceless constraint. In these schemes, special finite-differencing representations of the induction equations are implemented to preserve a particular numerical representation of the divergence of the magnetic field to roundoff error. In simulations using AMR grids, both constrained-transport schemes and the hyperbolic divergence-cleaning scheme [17,18] have been used. In the hyperbolic divergence-cleaning scheme, a generalized Lagrange multiplier (GLM) scalar is coupled to the system of MHD and induction equations. No special finite-differencing treatment is needed in solving the GLM-MHD system of equations. When they appear, divergence errors of the magnetic field are both propagated and damped away in the GLM-MHD scheme.

In the development of our AMR GRMHD code, we first tried the hyperbolic divergence-cleaning scheme, due to its straightforward implementation. We found that this scheme works well in the absence of black holes. One of the most commonly adopted methods for evolving black holes is the moving puncture technique [19,20], in which the physical singularity in the black hole interior is avoided by the use of the puncture gauge conditions. However, a coordinate singularity is present in the computational domain around which accurate numerical evolution is difficult to achieve. It has been demonstrated that the BSSN scheme, coupled with the puncture gauge conditions, guarantees that any inaccurate data in the black hole interior will not propagate out of the horizon [21–23]. We find that this property is preserved in the presence of hydrodynamic matter. However, it is no longer the case in the GLM-MHD scheme. In fact, we find that even in the Cowling approximation in which the metric is fixed, inaccurate data in the black hole interior can propagate out of the horizon in the GLM-MHD systems of equations. This problem may be overcome via black hole excision and applying appropriate ingoing boundary conditions at the excision boundary. (See [24] for a discussion of constraint preserving boundary conditions for Newtonian MHD.)

In developing an algorithm for maintaining $\boldsymbol{\nabla} \cdot \boldsymbol{B} = 0$ that is compatible with the moving puncture technique, we focused on constrained-transport schemes. That was the approach adopted in our earlier unigrid implementation [1]. A uniform-resolution, constrained-transport scheme may be used on each individual AMR refinement level. However, maintaining the divergenceless constraint at refinement level *boundaries* requires that special interpolations be performed during prolongation/restriction. Such prolongation/restriction operators have been devised [25,26], but must be fine-tuned to the particular AMR implementation. In this paper, we propose an alternative, AMR-compatible constrained-transport scheme. Our scheme is based on the constrained-transport scheme described in [27]. In this scheme, the magnetic induction equation is recast as an evolution equation for the magnetic vector potential. The divergence-free magnetic field is computed via the curl of the vector potential. The evolution of the vector potential is carried out in the same HRSC framework as other hydrodynamic variables. This scheme is numerically equivalent to the commonly used constrained-transport schemes based on a staggered-mesh algorithm [16]. This scheme is readily generalized to an AMR grid. Unlike the magnetic field, the vector potential is not constrained, and so any interpolation scheme can be used during prolongation and restriction, thus enabling its use with *any* AMR algorithm.

We have performed several tests on our new AMR constrained-transport scheme. We find that it works well even in black hole spacetimes. Inaccurate data generated in the black hole interior stay inside the horizon. Hence our scheme is compatible with the moving puncture technique.

The structure of this paper is as follows. In Sec. II, we describe our formalism, focusing on the derivation of the evolution equation for the magnetic vector potential. Then we describe our numerical scheme to evolve the coupled Einstein-Maxwell-MHD equations (Sec. III). Next we present several stringent code tests, including one- and two-dimensional shocks, magnetized Bondi accretion and the collapse of a magnetized rotating star (Sec. IV). Finally, we summarize our work in Sec. V and discuss applications of our new code to study various interesting problems in relativistic astrophysics.

II. FORMALISM

The formulation and numerical approach adopted in this paper are basically the same as those already reported in our previous work [1,11,12], to which the reader may refer for details. Here we introduce our notation, summarize our method, and focus on the derivation of the evolution equation for the magnetic vector potential in the ideal MHD limit, which is the basis of our new AMR constrained-transport scheme. Geometrized units ($G = c = 1$) are adopted throughout. Greek indices denote all four spacetime dimensions (0, 1, 2, and 3), and Latin indices imply spatial parts only (1, 2, and 3).

A. Metric evolution and gauge conditions

We use the standard 3 + 1 formulation of general relativity and decompose the metric into the following form:

$$ds^2 = -\alpha^2 dt^2 + \gamma_{ij}(dx^i + \beta^i dt)(dx^j + \beta^j dt). \quad (1)$$

The fundamental variables for the metric evolution are the spatial three-metric γ_{ij} and extrinsic curvature K_{ij}.

We adopt the BSSN formalism [2,3] in which the evolution variables are the conformal exponent $\phi \equiv \ln(\gamma)/12$, the conformal 3-metric $\tilde{\gamma}_{ij} = e^{-4\phi}\gamma_{ij}$, three auxiliary functions $\tilde{\Gamma}^i \equiv -\tilde{\gamma}^{ij}{}_{,j}$, the trace of the extrinsic curvature $K = \gamma_{ij}K^{ij}$, and the trace-free part of the conformal extrinsic curvature $\tilde{A}_{ij} \equiv e^{-4\phi}(K_{ij} - \gamma_{ij}K/3)$. Here, $\gamma = \det(\gamma_{ij})$ is the determinant of the spatial metric. The full spacetime metric $g_{\mu\nu}$ is related to the three-metric $\gamma_{\mu\nu}$ by $\gamma_{\mu\nu} = g_{\mu\nu} + n_\mu n_\nu$, where the future-directed, timelike unit vector n^μ normal to the time slice can be written in terms of the lapse α and shift β^i as $n^\mu = \alpha^{-1}(1, -\beta^i)$. The evolution equations of these BSSN variables are given by Eqs. (9)–(13) in [11]. It has been suggested that evolving $\chi = e^{-4\phi}$ or $W = e^{-2\phi}$ instead of ϕ gives more accurate results in binary black hole simulations (see e.g. [28–30]). Our code is capable of evolving these variables. Kreiss-Oliger dissipation is sometimes added in the BSSN evolution equations to reduce high-frequency numerical noise associated with AMR refinement interfaces [31]. It is also found that Kreiss-Oliger dissipation is sometimes useful in hydrodynamic simulations involving a black hole in a dynamical spacetime [12,32].

We adopt standard puncture gauge conditions to evolve the lapse and shift: an advective "1 + log" slicing condition for the lapse and a "Gamma-freezing" condition for the shift [33]. The evolution equations for these quantities are given by Eqs. 2, 3, and 4 in [12].

B. Evolution of electromagnetic fields

The electromagnetic stress-energy tensor $T^{\mu\nu}_{\rm em}$ is given by

$$T^{\mu\nu}_{\rm em} = \frac{1}{4\pi}\left(F^{\mu\lambda}F^{\nu}{}_{\lambda} - \frac{1}{4}g^{\mu\nu}F_{\alpha\beta}F^{\alpha\beta}\right). \tag{2}$$

We decompose the Faraday tensor $F^{\mu\nu}$ as

$$F^{\mu\nu} = n^\mu E^\nu - n^\nu E^\mu + n_\gamma \epsilon^{\gamma\mu\nu\delta}B_\delta, \tag{3}$$

so that E^μ and B^μ are the electric and magnetic fields measured by an observer normal to the spatial slice n^μ. Both fields are purely spatial ($E^\mu n_\mu = B^\mu n_\mu = 0$), and one can easily show that

$$E^\mu = F^{\mu\nu}n_\nu, \qquad B^\mu = \frac{1}{2}\epsilon^{\mu\nu\kappa\lambda}n_\nu F_{\lambda\kappa} = n_\nu F^{*\nu\mu}, \tag{4}$$

where

$$F^{*\mu\nu} = \frac{1}{2}\epsilon^{\mu\nu\kappa\lambda}F_{\kappa\lambda} \tag{5}$$

is the dual of $F^{\mu\nu}$.

Along with the electromagnetic field, we also assume the presence of a perfect fluid with rest-mass density ρ_0, pressure P, and 4-velocity u^μ, so that the total stress-energy tensor is

$$T^{\mu\nu} = \rho_0 h u^\mu u^\nu + P g^{\mu\nu} + T^{\mu\nu}_{\rm em}, \tag{6}$$

where the specific enthalpy h is related to the specific internal energy ϵ by $h = 1 + \epsilon + P/\rho_0$. The electric and magnetic fields measured by an observer comoving with the fluid are [cf. Eq. (4)]

$$E^\mu_{(u)} = F^{\mu\nu}u_\nu, \qquad B^\mu_{(u)} = u_\nu F^{*\nu\mu}. \tag{7}$$

For many applications of interest in relativistic astrophysics, one can assume perfect conductivity. In this ideal MHD limit, Ohm's law yields the MHD condition:

$$u_\mu F^{\mu\nu} = 0, \tag{8}$$

which is equivalent to the statement that the electric field observed in the fluid's rest frame vanishes ($E^\mu_{(u)} = 0$). In this limit, the total stress-energy tensor is given by

$$T^{\mu\nu} = (\rho_0 h + b^2)u^\mu u^\nu + \left(P + \frac{b^2}{2}\right)g^{\mu\nu} - b^\mu b^\nu, \tag{9}$$

where $b^\mu = B^\mu_{(u)}/\sqrt{4\pi}$ and $b^2 = b^\mu b_\mu$. The vector b^μ is related to B^μ by (see [1] for a derivation)

$$b^\mu = -\frac{P^\mu{}_\nu B^\nu}{n_\nu u^\nu \sqrt{4\pi}}, \tag{10}$$

where $P_{\mu\nu} = g_{\mu\nu} + u_\mu u_\nu$ is a projection tensor.

The evolution equation for the magnetic field in a perfectly conducting MHD fluid can be obtained in conservative form by taking the dual of Maxwell's equation $F_{[\mu\nu,\lambda]} = 0$. One finds

$$\nabla_\nu F^{*\mu\nu} = \frac{1}{\sqrt{-g}}\partial_\nu(\sqrt{-g}F^{*\mu\nu}) = 0, \tag{11}$$

where $\sqrt{-g} = \alpha\sqrt{\gamma}$. The time component of Eq. (11) gives the no-monopole constraint

$$\partial_j \tilde{B}^j = 0, \tag{12}$$

where

$$\tilde{B}^i = \sqrt{\gamma}B^i. \tag{13}$$

The spatial components of Eq. (11) give the magnetic induction equation, which can be written as

$$\partial_t \tilde{B}^i + \partial_j(v^j\tilde{B}^i - v^i\tilde{B}^j) = 0, \tag{14}$$

where $v^i = u^i/u^0$.

The induction equation can be recast as

$$\partial_t \tilde{B}^i = \tilde{\epsilon}^{ijk}\tilde{\epsilon}_{klm}\partial_j(v^l\tilde{B}^m), \tag{15}$$

where both $\tilde{\epsilon}^{ijk}$ and $\tilde{\epsilon}_{ijk}$ denote the permutation symbol, i.e. they are equal to 1 if ijk are in even permutation of (1,2,3), -1 if in odd permutation, and 0 if any two of the indices are equal. The divergenceless constraint (12) implies that $\tilde{B}^i$ can be derived from a vector potential A_i:

$$\tilde{B}^i = \tilde{\epsilon}^{ijk}\partial_j A_k. \tag{16}$$

It follows from Eqs. (13) and (16) that

$$B^i = \epsilon^{ijk}\partial_j A_k, \tag{17}$$

where $\epsilon^{ijk} = \tilde{\epsilon}^{ijk}/\sqrt{\gamma} = n_\mu \epsilon^{\mu ijk}$ is the three-dimensional Levi-Civita tensor associated with γ_{ij}. Equation (17) can be derived in a more general framework, as shown in [34].

The induction Eq. (15) will be satisfied automatically if A_i satisfies the evolution equation

$$\partial_t A_i = \tilde{\epsilon}_{ijk} v^j \tilde{B}^k. \tag{18}$$

It is clear that the evolution equations for A_i are not unique, since there are gauge degrees of freedom in the electromagnetic 4-vector potential. The general evolution equation for A_i in the ideal MHD limit is obtained by combining Eqs. (33) and (46) in [34]:

$$\partial_t A_i = \tilde{\epsilon}_{ijk} v^j \tilde{B}^k - \partial_i(\alpha\Phi - \beta^j A_j), \tag{19}$$

where Φ is the electromagnetic scalar potential. Hence the evolution Eq. (18) is equivalent to choosing the electromagnetic gauge condition

$$\Phi = \frac{1}{\alpha}(C + \beta^j A_j), \tag{20}$$

where C is a constant. In Minkowski spacetime, in which $\alpha = 1$ and $\beta^i = 0$, the gauge condition reduces to $\Phi = C$.

The scalar potential is only needed if one wishes to compute the electric field E^i. However, in the ideal MHD limit, the condition $u_\mu F^{\mu\nu} = 0$ relates E^i to B^i and v^i: $\alpha E_i = -\epsilon_{ijk}(v^j + \beta^j)B^k$. Therefore, it is not necessary to keep track of the scalar potential Φ in the ideal MHD limit.

In the nonrelativistic limit, Eq. (15) reduces to

$$\partial_t \boldsymbol{B} = \boldsymbol{\nabla} \times (\boldsymbol{v} \times \boldsymbol{B}) \tag{21}$$

and Eqs. (17) and (18) reduce to

$$\boldsymbol{B} = \boldsymbol{\nabla} \times \boldsymbol{A}, \qquad \partial_t \boldsymbol{A} = \boldsymbol{v} \times \boldsymbol{B}. \tag{22}$$

The ideal MHD condition becomes $\boldsymbol{E} = -\boldsymbol{v} \times \boldsymbol{B}$.

In our new AMR constrained-transport scheme, the induction equation is evolved via Eq. (18). The divergence-free magnetic field is then computed using Eq. (17). The numerical implementation will be described in Sec. III.

C. Evolution of the hydrodynamics fields

The stress-energy tensor for a magnetized plasma in the ideal MHD limit is

$$T^{\mu\nu} = (\rho_0 h + b^2)u^\mu u^\nu + \left(P + \frac{b^2}{2}\right)g^{\mu\nu} - b^\mu b^\nu. \tag{23}$$

Our evolution variables are

$$\rho_* \equiv -\sqrt{\gamma}\rho_0 n_\mu u^\mu, \tag{24}$$

$$\tilde{S}_i \equiv -\sqrt{\gamma}T_{\mu\nu}n^\mu \gamma^\nu{}_i, \tag{25}$$

$$\tilde{\tau} \equiv \sqrt{\gamma}T_{\mu\nu}n^\mu n^\nu - \rho_*. \tag{26}$$

The evolution equations are derived from the rest-mass conservation law $\nabla_\mu(\rho_0 u^\mu) = 0$ and conservation of energy-momentum $\nabla_\mu T^{\mu\nu} = 0$. These result in the continuity, momentum and energy equations [1]

$$\partial_t \rho_* + \partial_j(\rho_* v^j) = 0, \tag{27}$$

$$\partial_t \tilde{S}_i + \partial_j(\alpha\sqrt{\gamma}T^j{}_i) = \frac{1}{2}\alpha\sqrt{\gamma}T^{\alpha\beta}g_{\alpha\beta,i}, \tag{28}$$

$$\partial_t \tilde{\tau} + \partial_i(\alpha^2\sqrt{\gamma}T^{0i} - \rho_* v^i) = s, \tag{29}$$

where the source term in the energy equation is given by

$$\begin{aligned} s &= -\alpha\sqrt{\gamma}T^{\mu\nu}\nabla_\nu n_\mu \\ &= \alpha\sqrt{\gamma}[(T^{00}\beta^i\beta^j + 2T^{0i}\beta^j + T^{ij})K_{ij} \\ &\quad - (T^{00}\beta^i + T^{0i})\partial_i\alpha]. \end{aligned} \tag{30}$$

To complete the system of equations, the fluid equation of state (EOS) is specified. Our code currently implements a hybrid EOS of the form [35]

$$P(\rho_0, \epsilon) = P_{\rm cold}(\rho_0) + (\Gamma_{\rm th} - 1)\rho_0[\epsilon - \epsilon_{\rm cold}(\rho_0)], \tag{31}$$

where $P_{\rm cold}$ and $\epsilon_{\rm cold}$ denote the cold component of P and ϵ respectively, and $\Gamma_{\rm th}$ is a constant parameter which determines the conversion efficiency of kinetic to thermal energy at shocks. The function $\epsilon_{\rm cold}(\rho_0)$ is related to $P_{\rm cold}(\rho_0)$ by the first law of thermodynamics,

$$\epsilon_{\rm cold}(\rho_0) = \int \frac{P_{\rm cold}(\rho_0)}{\rho_0^2} d\rho_0. \tag{32}$$

In the code tests presented in this paper, we adopt the Γ-law EOS $P = (\Gamma - 1)\rho_0\epsilon$. This corresponds to setting $P_{\rm cold} = \kappa\rho_0^\Gamma$ (with constant κ) and $\Gamma_{\rm th} = \Gamma$.

III. NUMERICAL IMPLEMENTATION

We adopt Cartesian coordinates in our 3 + 1 simulations. Equatorial symmetry (i.e. symmetry with respect to the reflection $z \to -z$) is imposed when appropriate to save computational time. All the BSSN and hydrodynamical variables are stored at grid points (i, j, k). Magnetic field B^i and vector potential A_i are stored at staggered grid points as summarized in Table I.

The BSSN equations are evolved using a finite-differencing scheme. Our code currently supports second-, fourth-, and sixth-order spatial finite-differencing. In a spacetime containing black holes, we typically use a fourth- or sixth-order finite-differencing scheme. Our code is embedded in the Cactus parallelization framework [36], with time-stepping managed by the MOL (Method of Lines) thorn, which supports various explicit time-stepping

TABLE I. Storage location on grid of the magnetic field B^i and vector potential A_i.

Variable storage location	
B^x, $\tilde{B}^x$	$(i+\frac{1}{2}, j, k)$
B^y, $\tilde{B}^y$	$(i, j+\frac{1}{2}, k)$
B^z, $\tilde{B}^z$	$(i, j, k+\frac{1}{2})$
A_x	$(i, j+\frac{1}{2}, k+\frac{1}{2})$
A_y	$(i+\frac{1}{2}, j, k+\frac{1}{2})$
A_z	$(i+\frac{1}{2}, j+\frac{1}{2}, k)$

algorithms. Typically, we use the fourth-order Runge-Kutta method in time when evolving spacetimes containing black holes.

We use the Carpet [37] infrastructure to implement moving-box adaptive mesh refinement. In all AMR simulations presented here, second-order temporal prolongation is employed, coupled with fifth-order spatial prolongation for evolution variables stored on the unstaggered grid. The memory allocation for the staggered variables are the same as the unstaggered ones. The staggering is incorporated in our code in the evolution steps. Different spatial prolongation and restriction schemes have to be applied on the staggered evolution variables A_i to account for the different relative positions of these variables on adjacent refinement levels. We currently use a third-order Lagrangian scheme for interpolating these variables, but it can be easily generalized to other higher-order schemes, as well as more sophisticated schemes such as the essentially nonoscillatory (ENO) [38] and weighted essentially nonoscillatory (WENO) [39,40] schemes. We plan to investigate these alternative schemes in the future.

A. MHD evolution

The technique for evolving the BSSN equations is described in our earlier papers [11,12,41], so we focus here on our MHD evolution technique, which is based on an HRSC scheme. The goal of this part of the numerical evolution is to determine the fundamental MHD variables $\mathbf{P} = (\rho_0, P, v^i, B^i)$, called the *"primitive" variables*, at future times, given initial values of $\mathbf{P}$. The evolution equations (14) and (27)–(29) are written in conservative form:

$$\partial_t \boldsymbol{U} + \boldsymbol{\nabla} \cdot \boldsymbol{F} = \boldsymbol{S}, \tag{33}$$

where $\boldsymbol{U}(\boldsymbol{P}) = (\rho_*, \tilde{\tau}, \tilde{S}_i, \tilde{B}^i)$ are the "conserved" variables, and the flux $\boldsymbol{F}(\boldsymbol{P})$ and source $\boldsymbol{S}(\boldsymbol{P})$ do not contain derivatives of the primitive variables, although they are explicit functions of the metric and its derivatives.

Equation (33) may be evolved using a finite-volume or finite-difference scheme. A finite-volume scheme evolves the volume-averaged variables, whereas a finite-difference scheme evolves the point-valued variables. Our adopted constrained-transport scheme is based on a finite-volume algorithm. In a second-order scheme, there is no distinction between these two types of methods since the volume average and the gridpoint value are the same to second order. Since the metric is evolved using a finite-difference scheme, care must be taken to evolve the MHD and induction equations using a higher-order finite-volume scheme. One solution is to evolve the volume-averaged conservative variables $\bar{\boldsymbol{U}}$ from the point-value primitive variables $\boldsymbol{P}$ using a finite-volume algorithm. Next the updated point-value $\boldsymbol{U}$ is computed from the updated volume average quantity $\bar{\boldsymbol{U}}$ to the desired order of accuracy. The updated point-value $\boldsymbol{P}$ is then computed from the updated point-value $\boldsymbol{U}$ and metric quantities through primitives inversion. In this paper, we only consider second-order schemes for simplicity. Higher-order schemes are planned for the future, and important extra steps necessary to go beyond second order will be reviewed in this section.

Equation (33) can be written in a finite-volume form by integrating it over a cell volume. We obtain

$$\partial_t \bar{\boldsymbol{U}}_{i,j,k} + \frac{(\Delta_x \langle \boldsymbol{F} \rangle)_{i,j,k}}{\Delta x} + \frac{(\Delta_y \langle \boldsymbol{F} \rangle)_{i,j,k}}{\Delta y} + \frac{(\Delta_z \langle \boldsymbol{F} \rangle)_{i,j,k}}{\Delta z} = \bar{\boldsymbol{S}}_{i,j,k}, \tag{34}$$

where

$$(\Delta_x \langle \boldsymbol{F} \rangle)_{i,j,k} \equiv \langle \boldsymbol{F} \rangle_{i+(1/2),j,k} - \langle \boldsymbol{F} \rangle_{i-(1/2),j,k} \tag{35}$$

and similarly for operators Δ_y and Δ_z. We note that only a subset of $\boldsymbol{U}$, i.e. ρ_*, $\tilde{\tau}$ and $\tilde{S}_i$, is evolved using Eq. (34). The evolution of $\tilde{B}^i$ will be described in the next subsection. The bracket $\langle\rangle$ denotes a surface average. For example,

$$\langle \boldsymbol{F} \rangle_{i+(1/2),j,k} \equiv \frac{1}{\Delta y \Delta z} \int_{y_j^-}^{y_j^+} dy \int_{z_k^-}^{z_k^+} dz \boldsymbol{F}(x_i^+, y, z), \tag{36}$$

where $x_i^\pm = x_i \pm \Delta x/2$, $y_j^\pm = y_j \pm \Delta y/2$ and $z_k^\pm = z_k \pm \Delta z/2$. The fluxes $\langle \boldsymbol{F} \rangle_{i,j+(1/2),k}$ and $\langle \boldsymbol{F} \rangle_{i,j,k+(1/2)}$ are defined in the same way except that the surfaces to be averaged are in the x-z plane and x-y plane, respectively. The surface averaged flux $\langle \boldsymbol{F} \rangle$ and the point-value flux $\boldsymbol{F}$ are the same to second-order accuracy. To implement a higher-order scheme, one needs to compute not only the point-value $\boldsymbol{F}$ at the zone interface to the desired order, but also $\langle \boldsymbol{F} \rangle$ from the point-value $\boldsymbol{F}$ to the desired order of accuracy.

The computation of the fluxes is basically the same as described in [1]. It involves the reconstruction step and the Riemann solver step. In the reconstruction step, primitive variables at the zone interface are reconstructed. A slope-limited interpolation scheme from the zone center gives $\boldsymbol{P}_R$ and $\boldsymbol{P}_L$, the primitive variables at the right and left side of each zone interface, respectively. We usually employ the piecewise parabolic method (PPM) [42] or the monotonized central (MC) [43] reconstruction scheme, but in some problems involving strong discontinuities a more diffusive scheme such as the minmod reconstruction scheme must be used (see Sec. IV A 2). Since B^i is staggered (as shown in Table I), each B^i at one of the zone interfaces need not be

computed. From $\boldsymbol{P}_R$ and $\boldsymbol{P}_L$, we compute the fluxes $\boldsymbol{F}_R$ and $\boldsymbol{F}_L$, the "conservative" variables $\boldsymbol{U}_R$ and $\boldsymbol{U}_L$, as well as two pairs of characteristic velocities $c^R_\pm$ and $c^L_\pm$ at each zone interface (see Sec. IIIB of [1] for details).

The next step is the Riemann solver step. We employ the HLL (Harten, Lax, and van Leer) approximate Riemann solver [44] in which the HLL flux is given by

$$F^{\rm HLL} = \frac{c^- F_R + c^+ F_L - c^+ c^- (u_R - u_L)}{c^+ + c^-}, \tag{37}$$

where $c^\pm = \max(0, \pm c^R_\pm, \pm c^L_\pm)$. Our code also has the option of using the single-speed, local Lax-Friedrichs (LLF), or central-upwind, flux,

$$F^{\rm LLF} = \frac{1}{2}[F_R + F_L - c(u_R - u_L)], \tag{38}$$

where $c = \max(c^+, c^-)$.

The accuracy of the resulting flux depends on the reconstruction scheme and Riemann solver. In a smooth flow, MC reconstruction results in a second-order accurate point-value flux $\boldsymbol{F}$, whereas PPM is third order. However, these two schemes reduce to first order in a discontinuous flow (e.g. shocks) or at local extrema of $\boldsymbol{P}$. As mentioned above, even in a smooth flow where PPM gives third-order accurate point-value $\boldsymbol{F}$, $\langle \boldsymbol{F} \rangle$ has to be computed from the point-value $\boldsymbol{F}$ to third order to achieve an overall third-order accuracy.

B. Constrained-transport scheme

In this subsection, the standard constrained-transport scheme based on the staggered algorithm [16] is reviewed briefly. Next we introduce the vector potential method described in [27]. These two approaches give numerically identical results for schemes in which the time integration and spatial derivatives commute.

The evolution variables for the magnetic field in the standard constrained-transport scheme are the surface averaged field $\langle \tilde{B}^i \rangle$ defined in the same way as the surface averaged fluxes:

$$\langle \tilde{B}^x \rangle_{i+(1/2),j,k} \equiv \frac{1}{\Delta y \Delta z} \int_{y_j^-}^{y_j^+} dy \int_{z_k^-}^{z_k^+} dz \tilde{B}^x(x_i^+, y, z) \tag{39}$$

$$\langle \tilde{B}^y \rangle_{i,j+(1/2),k} \equiv \frac{1}{\Delta x \Delta z} \int_{x_i^-}^{x_i^+} dx \int_{z_k^-}^{z_k^+} dz \tilde{B}^y(x, y_j^+, z) \tag{40}$$

$$\langle \tilde{B}^z \rangle_{i,j,k+(1/2)} \equiv \frac{1}{\Delta x \Delta y} \int_{x_i^-}^{x_i^+} dx \int_{y_j^-}^{j_j^+} dy \tilde{B}^z(x, y, z_k^+). \tag{41}$$

Integrating the magnetic constraint equation $\partial_j \tilde{B}^j = 0$ over a cell volume gives the finite-volume equation for the constraint

$$\frac{(\Delta_x \langle \tilde{B}^x \rangle)_{i,j,k}}{\Delta x} + \frac{(\Delta_y \langle \tilde{B}^y \rangle)_{i,j,k}}{\Delta y} + \frac{(\Delta_z \langle \tilde{B}^z \rangle)_{i,j,k}}{\Delta z} = 0. \tag{42}$$

To derive the finite-volume equation for the magnetic induction equation, we first rewrite Eq. (15) as

$$\partial_t \tilde{B}^x = -\partial_y \mathcal{E}^z + \partial_z \mathcal{E}^y, \tag{43}$$

$$\partial_t \tilde{B}^y = -\partial_z \mathcal{E}^x + \partial_x \mathcal{E}^z, \tag{44}$$

$$\partial_t \tilde{B}^z = -\partial_x \mathcal{E}^y + \partial_y \mathcal{E}^x, \tag{45}$$

where

$$\mathcal{E}^x = -v^y \tilde{B}^z + v^z \tilde{B}^y, \tag{46}$$

$$\mathcal{E}^y = -v^z \tilde{B}^x + v^x \tilde{B}^z, \tag{47}$$

$$\mathcal{E}^z = -v^x \tilde{B}^y + v^y \tilde{B}^x. \tag{48}$$

We next define the line averaged $\mathcal{E}^i$ as

$$\hat{\mathcal{E}}^x_{i,j+(1/2),k+(1/2)} \equiv \frac{1}{\Delta x} \int_{x_i^-}^{x_i^+} \mathcal{E}^x(x, y_j^+, z_k^+) dx, \tag{49}$$

$$\hat{\mathcal{E}}^y_{i+(1/2),j,k+(1/2)} \equiv \frac{1}{\Delta y} \int_{y_j^-}^{y_j^+} \mathcal{E}^y(x_i^+, y, z_k^+) dy, \tag{50}$$

$$\hat{\mathcal{E}}^z_{i+(1/2),j+(1/2),k} \equiv \frac{1}{\Delta z} \int_{z_k^-}^{z_k^+} \mathcal{E}^z(x_i^+, y_j^+, z) dz. \tag{51}$$

Note that $\hat{\mathcal{E}}^i$ is staggered in the same way as A_i (see Table I). The finite-volume equations for the magnetic induction are obtained by integrating Eq. (43) over the cell surface normal to the x-direction, integrating Eq. (44) over the cell surface normal to the y-direction, and integrating Eq. (45) over the cell surface normal to the z-direction:

$$\partial_t \langle \tilde{B}^x \rangle_{i+(1/2),j,k} = \frac{(\Delta_z \hat{\mathcal{E}}^y)_{i+(1/2),j,k}}{\Delta z} - \frac{(\Delta_y \hat{\mathcal{E}}^z)_{i+(1/2),j,k}}{\Delta y}, \tag{52}$$

$$\partial_t \langle \tilde{B}^y \rangle_{i,j+(1/2),k} = \frac{(\Delta_x \hat{\mathcal{E}}^z)_{i,j+(1/2),k}}{\Delta x} - \frac{(\Delta_z \hat{\mathcal{E}}^x)_{i,j+(1/2),k}}{\Delta z}, \tag{53}$$

$$\partial_t \langle \tilde{B}^z \rangle_{i,j,k+(1/2)} = \frac{(\Delta_y \hat{\mathcal{E}}^x)_{i,j,k+(1/2)}}{\Delta y} - \frac{(\Delta_x \hat{\mathcal{E}}^y)_{i,j,k+(1/2)}}{\Delta x}. \tag{54}$$

It is straightforward to verify that Eqs. (52)–(54) imply that the time derivative of the left-hand side of Eq. (42) vanishes. Hence a finite-volume scheme that evolves Eqs. (52)–(54) preserves the constraint (42) to roundoff error, provided that the initial data $\langle \tilde{B}^i \rangle$ satisfy the constraint.

To evolve Eqs. (52)–(54), $\mathcal{E}$ has to be computed at the zone edge. The computation is similar to that of the flux $\boldsymbol{F}$ described in the previous subsection. Since B^i is staggered (as specified in Table I), computation of each $\mathcal{E}^i$ at the zone edge requires reconstruction of B^i along one direction. However, since v^i is stored at the zone center, two

independent one-dimensional reconstructions are necessary, as pointed out in [27]. The HLL and Lax-Friedrichs formulas for $\mathcal{E}^z$ at the zone edge are given by [27]

$$(\mathcal{E}^z)^{\rm HLL} = \frac{c_x^+ c_y^+ \mathcal{E}^z_{LL} + c_x^+ c_y^- \mathcal{E}^z_{LR} + c_x^- c_y^- \mathcal{E}^z_{RL} + c_x^- c_y^- \mathcal{E}^z_{RR}}{(c_x^+ + c_x^-)(c_y^+ + c_y^-)} + \frac{c_x^+ c_x^-}{c_x^+ + c_x^-}(\tilde{B}^y_R - \tilde{B}^y_L) - \frac{c_y^+ c_y^-}{c_y^+ + c_y^-}(\tilde{B}^x_R - \tilde{B}^x_L) \tag{55}$$

and

$$(\mathcal{E}^z)^{\rm LLF} = \frac{1}{4}(\mathcal{E}^z_{LL} + \mathcal{E}^z_{LR} + \mathcal{E}^z_{RL} + \mathcal{E}^z_{RR}) + \frac{c_x}{2}(\tilde{B}^y_R - \tilde{B}^y_L) - \frac{c_y}{2}(\tilde{B}^x_R - \tilde{B}^x_L), \tag{56}$$

which are the generalizations of Eqs. (37) and (38). In the above formulas, $\mathcal{E}^z_{LR}$ denotes the reconstructed left state in the x-direction and right state in the y-direction. Other symbols involving $\mathcal{E}^z$ are interpreted in the similar fashion. $\tilde{B}^y_R$ and $\tilde{B}^y_L$ denote the reconstructed right and left state of $\tilde{B}^y$ in the x-direction; $\tilde{B}^x_R$ and $\tilde{B}^x_L$ denote the reconstructed right and left state in the y-direction. The $c_x^\pm$ and $c_y^\pm$ should be computed by taking the maximum characteristic speed among the four reconstructed states. However, we set them equal to the maximum over the two neighboring interface values for simplicity, as suggested in [27]. In the LLF formula, c_x and c_y are set to the maximum of $c_x^\pm$ and $c_y^\pm$, respectively. The formula for $(\mathcal{E}^x)^{\rm HLL}$ is obtained from Eq. (55) by permuting the indices $z \to x$, $x \to y$ and $y \to z$, whereas the formula for $(\mathcal{E}^y)^{\rm HLL}$ is obtained from Eq. (55) by permuting the indices $z \to y$, $x \to z$ and $y \to x$. The same rule applies for $(\mathcal{E}^x)^{\rm LLF}$ and $(\mathcal{E}^y)^{\rm LLF}$. The reconstructed point-value $\mathcal{E}^i$ at the zone edge is the same as the line averaged value $\hat{\mathcal{E}}^i$ to second order. If one wishes to go beyond second order, $\hat{\mathcal{E}}^i$ has to be computed from $\mathcal{E}^i$ to the desired order of accuracy.

We now describe the vector potential method proposed in [27], which has been adopted for our AMR constrained-transport scheme. We first define the line averaged vector potential $\hat{A}_i$ exactly the same way as $\hat{\mathcal{E}}^i$:

$$(\hat{A}_x)_{i,j+(1/2),k+(1/2)} \equiv \frac{1}{\Delta x}\int_{x_i^-}^{x_i^+} A_x(x, y_j^+, z_k^+)dx, \tag{57}$$

$$(\hat{A}_y)_{i+(1/2),j,k+(1/2)} \equiv \frac{1}{\Delta y}\int_{y_j^-}^{y_j^+} A_y(x_i^+, y, z_k^+)dy, \tag{58}$$

$$(\hat{A}_z)_{i+(1/2),j+(1/2),k} \equiv \frac{1}{\Delta z}\int_{z_k^-}^{z_k^+} A_z(x_i^+, y_j^+, z)dz. \tag{59}$$

It follows from Eq. (16) that

$$\langle\tilde{B}^x\rangle_{i+(1/2),j,k} = \frac{(\Delta_y \hat{A}_z)_{i+(1/2),j,k}}{\Delta y} - \frac{(\Delta_z \hat{A}_y)_{i+(1/2),j,k}}{\Delta z}, \tag{60}$$

$$\langle\tilde{B}^y\rangle_{i,j+(1/2),k} = \frac{(\Delta_z \hat{A}_x)_{i,j+(1/2),k}}{\Delta z} - \frac{(\Delta_x \hat{A}_z)_{i,j+(1/2),k}}{\Delta x}, \tag{61}$$

$$\langle\tilde{B}^z\rangle_{i,j,k+(1/2)} = \frac{(\Delta_x \hat{A}_y)_{i,j,k+(1/2)}}{\Delta x} - \frac{(\Delta_y \hat{A}_x)_{i,j,k+(1/2)}}{\Delta y}. \tag{62}$$

It is easy to verify that the data $\langle\tilde{B}^i\rangle$ generated from $\hat{A}_i$ from the above formulas satisfy the constraint (42). In the vector potential method, the evolution variable is $\hat{A}_i$. The evolution equation is derived from Eq. (18) and is given by

$$\partial_t(\hat{A}_x)_{i,j+(1/2),k+(1/2)} = -\hat{\mathcal{E}}^x_{i,j+(1/2),k+(1/2)}, \tag{63}$$

$$\partial_t(\hat{A}_y)_{i+(1/2),j,k+(1/2)} = -\hat{\mathcal{E}}^y_{i+(1/2),j,k+(1/2)}, \tag{64}$$

$$\partial_t(\hat{A}_z)_{i+(1/2),j+(1/2),k} = -\hat{\mathcal{E}}^z_{i+(1/2),j+(1/2),k}. \tag{65}$$

The value of $\mathcal{E}^i$ at the zone edge is computed in exactly the same way as the standard constrained-transport scheme, i.e., by using Eq. (55) or Eq. (56) for $\mathcal{E}^z$ and similar formulas for $\mathcal{E}^x$ and $\mathcal{E}^y$. Having evolved $\hat{A}_i$, the updated conservative variables $\langle\tilde{B}^i\rangle$ are computed using Eqs. (60)–(62). The divergence of $\langle\tilde{B}^i\rangle$ is therefore automatically guaranteed to be zero to roundoff error.

It is apparent that the vector potential method and the standard constrained-transport scheme are closely related. They both apply the same procedure of computing $\mathcal{E}^i$ at the zone edge. They both involve taking spatial derivatives (more precisely, the discretized curl operator) via the differencing operators Δ_x, Δ_y and Δ_z. The only difference between these two methods is that in the standard constrained-transport scheme, spatial derivatives are applied before time integration, whereas in the vector potential method spatial derivatives are applied after time integration. Since we employ the MoL algorithm in which spatial derivatives and time integration commute, the two methods give numerically identical results in simulations using a uniformly-spaced grid. We prefer to use the vector potential method in AMR simulations since A_i is not constrained and so does not require special interpolation schemes during prolongation and restriction.

During the MHD evolution steps, values of B^i at the zone center are also needed, which are currently computed by simply taking the average of B^i on the staggered grid. Taking the limit $\Delta x^i \to 0$ in Eq. (42), we see that $\langle\tilde{B}^i\rangle$ is always continuous in the x^i direction (e.g., even in the presence of shocks). Thus the averaging scheme generally gives a second-order accurate B^i at the zone center. Higher-order schemes will require more sophisticated interpolation algorithms.

C. Recovery of primitive variables

Having computed $\mathbf{U}$ at the new timestep, we need to recover $\mathbf{P}$, the primitive variables on the new time level. This is not trivial because, although the relations $\mathbf{U}(\mathbf{P})$ are

analytic, the inverse relations $\mathbf{P}(\mathbf{U})$ are not. For a Γ-law EOS $P = (\Gamma - 1)\rho_0\epsilon$, the inversion can be reduced to an eighth-order polynomial equation [27,45]. In the absence of a magnetic field, the equation can be further reduced to a quartic equation where an analytic solution is available. However, for a general EOS, the inversion must be solved numerically. Various inversion algorithms are studied extensively in [45], and it has been found that the most efficient inversion technique is to solve two coupled nonlinear equations using the Newton-Raphson scheme.

Our code supports three inversion schemes: the optimal 2D scheme described in [45], a slightly modified analytic quartic solver from the GNU Scientific Library (used for a Γ-law EOS in the absence of magnetic field), and our older scheme that solves four coupled nonlinear algebraic equations.

D. Black hole interior

We use the moving puncture technique to evolve spacetimes containing black holes. The black hole spacetime singularity is avoided by the puncture gauge conditions, but a coordinate singularity (i.e. puncture) remains in the interior of each black hole on the computational domain. One nice property of the moving puncture method is that, although accurate evolution near the puncture is not maintained, inaccurate data do not propagate out of the black hole horizon. This method proves to be robust in the evolution of binary black holes and is widely used in the numerical relativity community. The moving puncture method has also been used in simulations involving hydrodynamic matter and MHD (see e.g., [10,12,13,32,46–48]).

One difficulty in handling MHD in the black hole interior is the loss of accuracy near the puncture. This can drive the conservative variables $\boldsymbol{U}$ out of physical range, resulting in unphysical primitive variables after inversion (e.g. negative pressure or even complex solutions). In the absence of magnetic fields, this can be avoided by enforcing the constraints [11]

$$|\tilde{S}|^2 \equiv \gamma^{ij}\tilde{S}_i\tilde{S}_j < \tilde{\tau}(\tilde{\tau} + 2\rho_*), \quad \text{and} \tag{66}$$

$$\tilde{\tau} > 0. \tag{67}$$

When the second condition is not met, we reset τ to a small positive number. When the first condition is violated we rescale $\tilde{S}_i$ so that its new magnitude is $|\tilde{S}|^2 = f\tilde{\tau}(\tilde{\tau} + 2\rho_*)$, where $f \leq 1$ is a parameter. This technique does not apply in the presence of magnetic fields. We instead apply a fix, first suggested by Font *et al.* [49], which consists of replacing the energy equation (29) by the cold EOS, $P = P_{\rm cold}(\rho_0)$ when solving the system of equations. This substitution guarantees a positive pressure. In rare cases, this revised system also fails to give a solution and we repair the zone by averaging from nearby zones (averaging is not applied to the magnetic field).

When matter and magnetic fields fall into the black hole, the energy density near the puncture can be very high. This results in a large energy source term in the BSSN equation, which can cause the conformal related metric $\tilde{\gamma}_{ij}$ to lose positive definiteness near the puncture. This behavior eventually causes the code to crash. Hence, other techniques are sometimes used to stabilize the evolution in the black hole interior. For example, adding a Kreiss-Oliger dissipation in the black hole interior is found to be useful [12,32], as well as setting an upper and lower limit on the pressure. In some MHD simulations, we find that setting the magnetic field to zero deep inside the horizon can stabilize the evolution (see Sec. IV C).

E. Low-density regions

If a pure vacuum were to exist anywhere in our computational domain, the MHD approximation would not apply in this region, and the vacuum Maxwell equations would need to be solved there. In many astrophysical scenarios, however, a sufficiently dense, ionized plasma will exist outside the stars or disks, where MHD will remain valid in its force-free limit. As in many hydrodynamic and MHD simulations, we add a tenuous "atmosphere" to cover the computational grid outside the star or disk. We maintain a density and pressure floor $\rho_{\rm atm}$ and $P_{\rm atm}$ in the atmosphere. We usually set $\rho_{\rm atm} = 10^{-10}\rho_{\rm max}(0)$ and $P_{\rm atm} = P_{\rm cold}(\rho_{\rm atm})$, where $\rho_{\rm max}(0)$ is the maximum rest-mass density in the initial data. Throughout the evolution, we impose limits on the atmospheric pressure to prevent spurious heating and negative values of the internal energy when the density ρ_0 is smaller than a threshold $\rho_{\rm th}$. Specifically, we require $P_{\rm min}(\rho_0) \leq P \leq P_{\rm max}(\rho_0)$, where $P_{\rm max}(\rho_0) = 10P_{\rm cold}(\rho_0)$ and $P_{\rm min}(\rho_0) = P_{\rm cold}(\rho_0)/2$ when $\rho_0 < \rho_{\rm th}$. The value of $\rho_{\rm th}$ is usually set between $10\rho_{\rm atm}$ and $100\rho_{\rm atm}$. Setting $\rho_{\rm th}$ too high could cause unphysical effects in a simulation, such as spurious angular momentum loss [12].

F. Boundary conditions

In simulations in which the spacetime is asymptotically flat, we apply Sommerfeld outgoing wave boundary conditions to the BSSN and gauge variables $\mathbf{f}$, i.e.,

$$\mathbf{f}(r, t) = \frac{r - \Delta r}{r}\mathbf{f}(r - \Delta r, t - \Delta T) \tag{68}$$

at the outer boundary of our numerical grid. Here ΔT is the timestep and $\Delta r = \alpha e^{-2\phi}\Delta T$. In simulations in which hydrodynamic matter and plasma are initially localized, outflow boundary conditions are imposed on the hydrodynamic variables ρ_0, v^i and P (i.e., the variables are copied along the grid directions with the condition that the velocities be positive or zero in the outer grid zones). For the magnetic field, we compute A_i at the outer boundaries by either linear or quadratic extrapolation. The linear extrapolation is equivalent to copying $\tilde{B}^i$ to the outer

boundary, whereas the quadratic extrapolation corresponds to linearly extrapolating $\tilde{B}^i$ to the outer boundary.

Other boundary conditions are used in the code tests presented in this paper, which will be specified in each case.

IV. CODE TESTS

A. Minkowski spacetime MHD tests

1. One-dimensional tests

We perform a suite of one-dimensional MHD tests in Minkowski spacetime, as described in [50]. The initial configurations of the tests are summarized in Table II. We only perform tests in which analytic solutions are available. In these 1D tests, all variables are functions of x only. The divergenceless constraint $\boldsymbol{\nabla} \cdot \boldsymbol{B} = 0$ implies that B^x is a constant. For these tests, the initial magnetic field $\boldsymbol{B}$ can be derived from the following vector potential:

$$A_x(x) = 0, \tag{69}$$

$$A_y(x) = \int_0^x B^z(x')dx', \tag{70}$$

$$A_z(x) = yB^x - \int_0^x B^y(x')dx'. \tag{71}$$

We integrate the MHD equations from $t = 0$ to $t = t_{\rm final}$, where $t_{\rm final}$ is specified in Table II for each case. The gas satisfies a Γ-law EOS with $\Gamma = 4/3$, and is evolved on a uniform resolution grid with $\Delta x = 0.01$. We are able to integrate all the cases using the PPM reconstruction scheme and the HLL approximate Riemann solver with a timestep $\Delta t = 0.5\Delta x$. We use "copy" boundary conditions (i.e. hydrodynamic variables are copied and the vector potential is linearly extrapolated to the boundary points) in all cases. The first 6 tests in Table II start with discontinuous initial data at $x = 0$, with homogeneous profiles on either side. Figs. 1–3 show the profiles of ρ_0 and u^x at time $t = t_{\rm final}$. Notice that the numerical results agree very well with the analytic solution in all cases. The overall performance of the new MHD scheme in these tests is about as good as our old constrained-transport scheme presented in [1].

In the nonlinear Alfvén wave test, unlike the first 6 tests, the two states listed in Table II are joined by a continuous function. We use the same initial data described in Appendix B of [1]. Figure 4 demonstrates very good agreement between numerical results and the analytic solution for velocity and magnetic field profiles at time $t = t_{\rm final} = 2$. Figure 5 shows the L2 norm of the error in u^x, u^y, B^y and B^z, varying only numerical resolution. The L2 norm of a grid function $\delta g \equiv g - g^{\rm exact}$ is computed by summing over every grid point i:

TABLE II. Initial states for 1D MHD tests.[a]

Test	Left state	Right State	$t_{\rm final}$
Fast Shock	$u^i = (25.0, 0.0, 0.0)$	$u^i = (1.091, 0.3923, 0.00)$	2.5
	$B^i/\sqrt{4\pi} = (20.0, 25.02, 0.0)$	$B^i/\sqrt{4\pi} = (20.0, 49.0, 0.0)$	
	$P = 1.0,\ \rho_0 = 1.0$	$P = 367.5,\ \rho_0 = 25.48$	
Slow Shock	$u^i = (1.53, 0.0, 0.0)$	$u^i = (0.9571, -0.6822, 0.00)$	2.0
	$B^i/\sqrt{4\pi} = (10.0, 18.28, 0.0)$	$B^i/\sqrt{4\pi} = (10.0, 14.49, 0.0)$	
	$P = 10.0,\ \rho_0 = 1.0$	$P = 55.36,\ \rho_0 = 3.323$	
Switch-off Fast	$u^i = (-2.0, 0.0, 0.0)$	$u^i = (-0.212, -0.590, 0.0)$	1.0
Rarefaction	$B^i/\sqrt{4\pi} = (2.0, 0.0, 0.0)$	$B^i/\sqrt{4\pi} = (2.0, 4.71, 0.0)$	
	$P = 1.0,\ \rho_0 = 0.1$	$P = 10.0,\ \rho_0 = 0.562$	
Switch-on Slow	$u^i = (-0.765, -1.386, 0.0)$	$u^i = (0.0, 0.0, 0.0)$	2.0
Rarefaction	$B^i/\sqrt{4\pi} = (1.0, 1.022, 0.0)$	$B^i/\sqrt{4\pi} = (1.0, 0.0, 0.0)$	
	$P = 0.1,\ \rho_0 = 1.78 \times 10^{-3}$	$P = 1.0,\ \rho_0 = 0.01$	
Shock Tube 1	$u^i = (0.0, 0.0, 0.0)$	$u^i = (0.0, 0.0, 0.0)$	1.0
	$B^i/\sqrt{4\pi} = (1.0, 0.0, 0.0)$	$B^i/\sqrt{4\pi} = (1.0, 0.0, 0.0)$	
	$P = 1000.0,\ \rho_0 = 1.0$	$P = 1.0,\ \rho_0 = 0.1$	
Shock Tube 2	$u^i = (0.0, 0.0, 0.0)$	$u^i = (0.0, 0.0, 0.0)$	1.0
	$B^i/\sqrt{4\pi} = (0.0, 20.0, 0.0)$	$B^i/\sqrt{4\pi} = (0.0, 0.0, 0.0)$	
	$P = 30.0,\ \rho_0 = 1.0$	$P = 1.0,\ \rho_0 = 0.1$	
Nonlinear Alfvén wave[b]	$u^i = (0.0, 0.0, 0.0)$	$u^i = (3.70, 5.76, 0.00)$	2.0
	$B^i/\sqrt{4\pi} = (3.0, 3.0, 0.0)$	$B^i/\sqrt{4\pi} = (3.0, -6.857, 0.0)$	
	$P = 1.0,\ \rho_0 = 1.0$	$P = 1.0,\ \rho_0 = 1.0$	

[a]In all cases, the gas satisfies the Γ-law EOS with $\Gamma = 4/3$. For the first 6 tests, the left state refers to $x < 0$ and the right state, $x > 0$.
[b]For the nonlinear Alfvén wave, the left and right states are joined by a continuous function. See [51] or Appendix B of [1] for details.

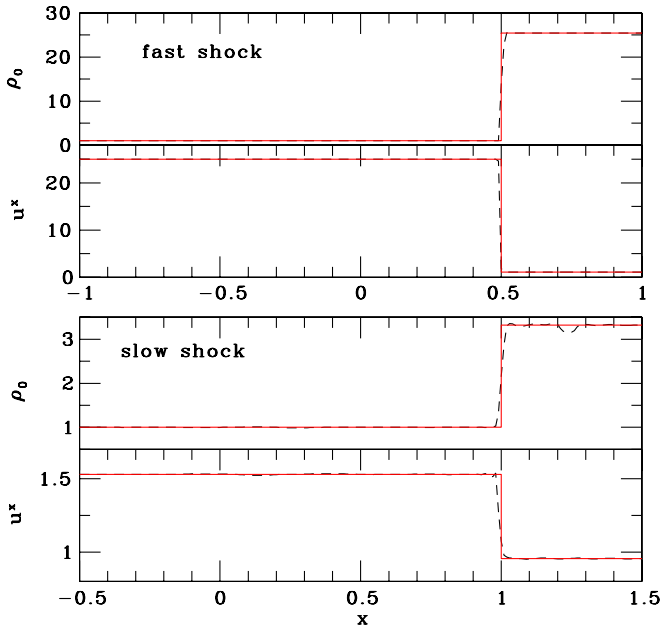

FIG. 1 (color online). 1D fast and slow shock density and velocity profiles, at $t = t_{\rm final}$ (see Table II). Data from numerical simulations with resolution $\Delta x = 0.01$ are plotted with dashed (black) lines, and solid (red) lines denote the analytic solutions.

$$\mathrm{L}\,2(\delta g) = \sqrt{\sum_{i=1}^{N} [\delta g(x_i)]^2 \Delta x}, \tag{72}$$

where $N \propto 1/\Delta x$ is the number of grid points. We find that the errors converge to zero at second order in Δx, as expected.

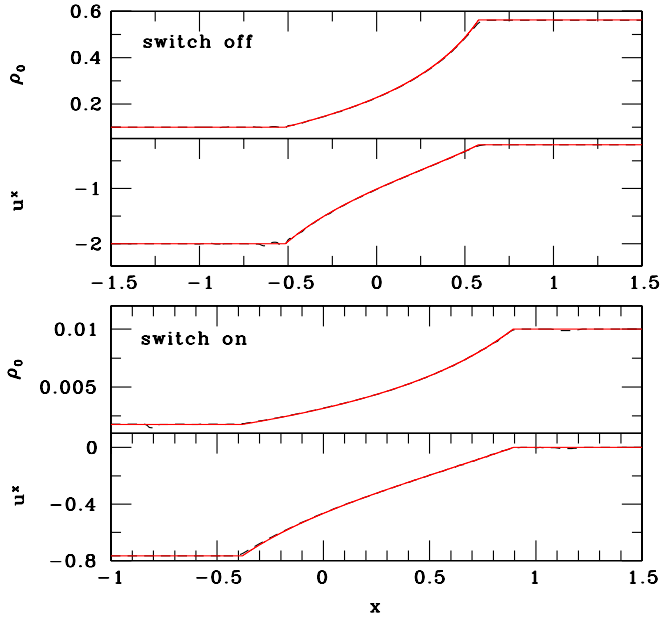

FIG. 2 (color online). Same as Fig. 1 but for the 1D switch-off and switch-on tests.

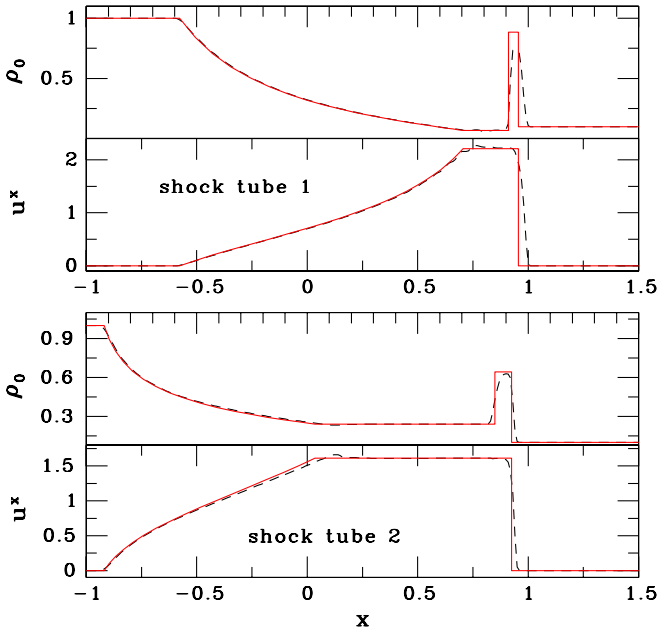

FIG. 3 (color online). Same as Fig. 1 but for the 1D shock tube 1 and shock tube 2 tests.

2. Two-dimensional tests

We perform the two-dimensional cylindrical blast explosion test and rotating disk test described in [15,27].

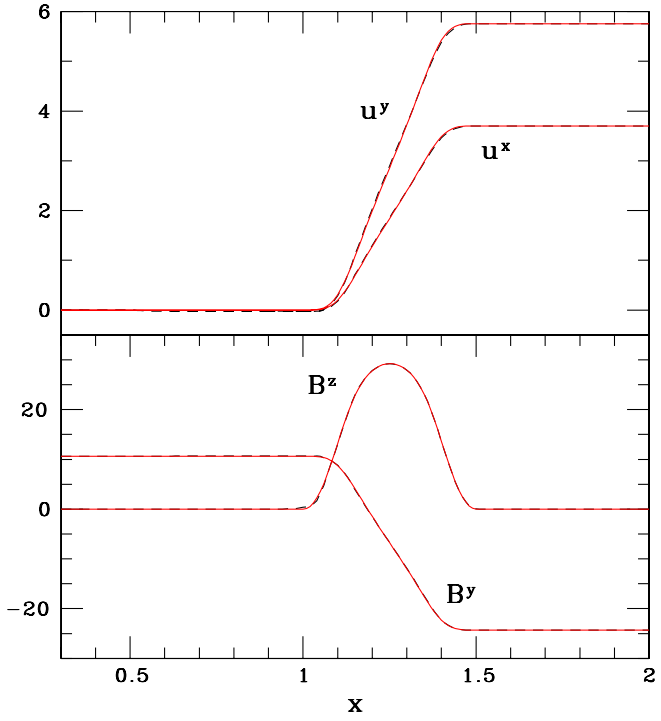

FIG. 4 (color online). 1D nonlinear Alfvén wave test: MHD variable profiles. Test results with resolution $\Delta x = 0.01$ (dashed, black lines) are compared to the exact solution (solid, red lines) at time $t = t_{\rm final} = 2.0$. Our computational domain is $x \in (-2, 2)$.

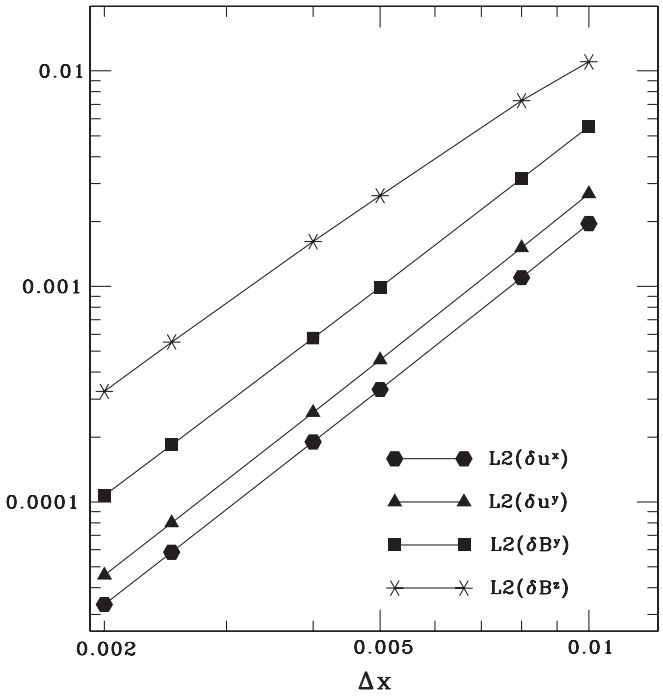

FIG. 5. 1D nonlinear Alfvén wave test: L2 norms of the errors in u^x, u^y, B^y and B^z at $t = t_{\rm final} = 2.0$. This log-log plot demonstrates that L2 norms of the errors are proportional to Δx^2, and are thus second-order convergent.

In both tests, all variables are functions of x and y only, the initial magnetic field is uniform and oriented along the x-direction, and the initial velocity does not have the z-component. Such a uniform magnetic field can be derived from the vector potential

$$A_x = A_y = 0, \qquad A_z = yB^x. \tag{73}$$

It can be shown from the MHD evolution equations that $A_x = A_y = B^z = v^z = 0$ remains true for all time t. It can also been shown from the finite-volume equations that our MHD evolution scheme preserves this property. Our numerical simulations also confirm that $A_x = A_y = B^z = v^z = 0$ is satisfied to roundoff error at all times. It follows from $A_x = A_y = B^z = 0$ and $\boldsymbol{B} = \boldsymbol{\nabla} \times \boldsymbol{A}$ that $B^i \partial_i A_z = 0$. Hence contours of constant A_z coincide with the magnetic field lines. The evolution of magnetic field thus reduces to the evolution of A_z, which can be shown to satisfy the simple advection equation:

$$\partial_t A_z + v^i \partial_i A_z = 0. \tag{74}$$

It follows from Eq. (74) that the constant A_z contours are comoving with the fluid. We note that we do not evolve Eq. (74) directly. Instead, we evolve A_z using the HRSC scheme described in Sec. III B. Small numerical resistivity inherent in our HRSC scheme could cause small violations of Eq. (74), especially in regions of strong shocks. However, the relation $B^i \partial_i A_z = 0$ is satisfied to truncation error at all times.

Cylindrical blast explosion.—In this test, the fluid is initially at rest with uniform density $\rho_0 = 1$ throughout the computational domain $x \in (-0.55, 0.55)$, $y \in (-0.55, 0.55)$. Inside a cylinder of radius 0.08 is a uniform high pressure $P = 10^4$ surrounded by an ambient fluid of much lower pressure $P = 0.1$. The initial magnetic field is $B^x/\sqrt{4\pi} = 4.0$, and $B^y = B^z = 0$ everywhere. The fluid satisfies a Γ-law EOS with $\Gamma = 4/3$. We perform simulations with uniform resolutions $\Delta x = \Delta y \equiv \Delta = 0.004$, 0.0025 and 0.002, applying copy boundary conditions at the computational domain boundaries. We find that evolutions with HLL flux, coupled with either the MC or PPM reconstruction schemes, result in a code crash due to the strong initial pressure jump. We are able to evolve the system stably by using the minmod reconstruction scheme coupled with the LLF flux. A similar finding is reported in [52].

Figure 6 shows the two-dimensional profile of density ρ_0, gas pressure P, magnetic pressure $b^2/2$ and magnetic field lines at time $t = 0.4$, where the blast wave has nearly reached the boundary of the computational domain. Figure 7 shows the one-dimensional profiles along the x and y axis for the three resolutions. The profiles are qualitatively similar to the those reported in [27,50,52]. The initial high pressure in the central region causes a strong explosion. The explosion is asymmetric in the

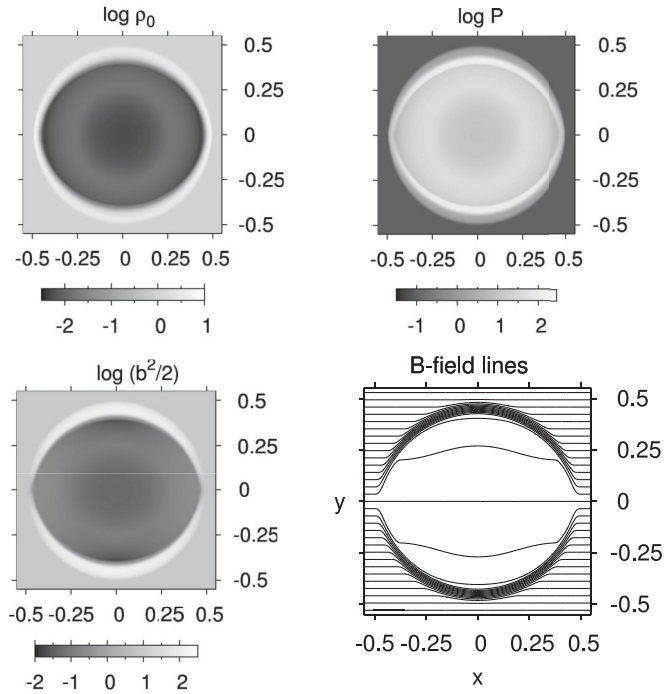

FIG. 6. Cylindrical blast explosion: 2D MHD variable profiles. Density ρ_0, gas pressure P, magnetic pressure $b^2/2$, and magnetic field lines are plotted at $t = 0.4$. The simulation is performed with uniform resolution $\Delta x = \Delta y \equiv \Delta = 0.002$. Magnetic field lines coincide with contours of A_z, and are thus plotted according to $A_z = 0.5i - 8$, with $i = 1, 2, \ldots, 31$.

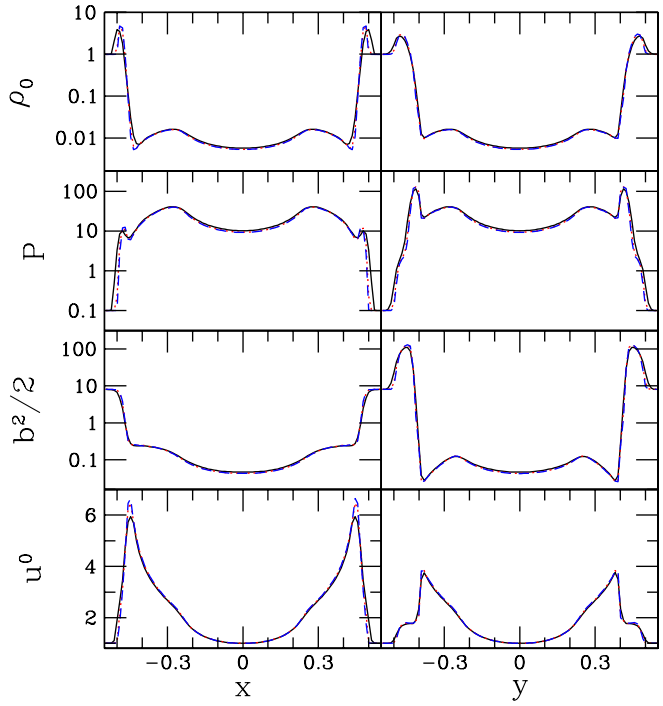

FIG. 7 (color online). Cylindrical blast explosion test: 1D MHD variable profiles at different resolutions. Density ρ_0, pressure P, magnetic pressure $b^2/2$, and Lorentz factor u^0 profiles along the x-axis (left) and y-axis (right) at $t = 0.4$ are plotted at resolutions $\Delta = 0.004$ (black solid line), 0.0025 (red dotted line) and 0.002 (blue dashed line).

x- and y-directions due to the presence of magnetic fields. The explosion is unimpeded in the x-direction, so the Lorentz factor u^0 of the fluid is larger along the x-axis than along the y-axis, as demonstrated in Fig. 7. The magnetic field lines are squeezed in the y direction, sapping the magnetic field energy in the central region, and driving an intense magnetic field in two thin oblate layers surrounding the central region (see Fig. 6). By $t = 0.4$, the central density and magnetic pressure have decreased by 2 orders of magnitude, while the central gas pressure has dropped by 3 orders of magnitude.

By comparing the numerical data from the three resolution runs in the entire computational domain at $t = 0.4$, we see signs of convergence. However, the convergence rate is less than first order. This is likely due to the fact that the initial strong pressure discontinuity requires resolutions higher than those used in our simulations to exhibit the proper convergence, as pointed out in [52]. However, we find that in the central $|x| < 0.3$, $|y| < 0.3$ region, ρ_0, P and b^2 converge to second order, while u^0 converges to first order.

Cylindrical rotating disk (rotor).—The initial configuration of this rotor test consists of a uniform high-density ($\rho_0 = 10$) central region of cylindrical radius 0.1 uniformly rotating with an angular velocity $\omega = 9.95$. The disk is surrounded by an ambient gas of density $\rho_0 = 1$. The gas pressure $P = 1$ is constant everywhere. The initial magnetic field is uniform and is set to $B^x/\sqrt{4\pi} = 1$ and $B^y = B^z = 0$. The gas satisfies a $\Gamma = 5/3$ EOS. We evolve the system using the minmod reconstruction scheme coupled with the LLF flux and at resolutions $\Delta x = \Delta y = \Delta = 0.004$, 0.0025 and 0.002. Copy boundary conditions are applied at the outer boundaries for this test.

Figures 8 and 9 show the profiles of ρ_0, P, $b^2/2$, u^0 and magnetic field lines at time $t = 0.4$. These profiles are qualitatively similar to those in [27,52]. The rotor causes magnetic winding. At time $t = 0.4$, the field lines in the central region are rotated by $\sim 90°$. The winding slows down the rotation of the disk. The maximum Lorentz factor decreases from the initial value of 10 to 1.7 at $t = 0.4$. The density, pressure and magnetic field in the central region also decrease substantially. A high-density, oblate shell is formed surrounding the central region.

As in the cylindrical explosion test, we see signs of convergence as the resolution is increased. However, the overall convergence rate is less than first order due to resolutions too low to adequately resolve the fine structure of the flow. The rotor test is even more severe than the cylindrical explosion test. This is because the initial Lorentz factor u^0 has a steep slope near the edge of the disk. Even with our highest resolution $\Delta = 0.002$, the

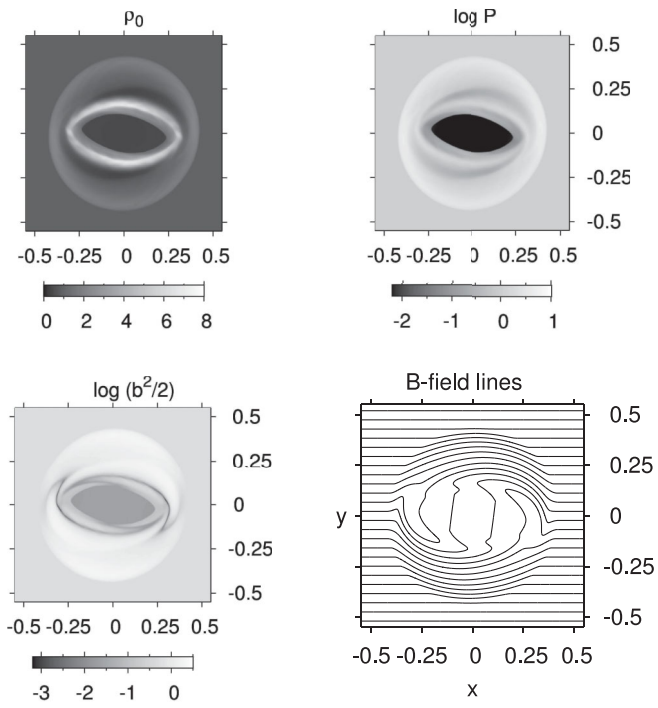

FIG. 8. Cylindrical rotating disk (rotor) test: 2D MHD variable profiles. Density ρ_0, gas pressure P, magnetic pressure $b^2/2$, and magnetic field lines are plotted on the xy-plane at $t = 0.4$. The simulation is performed with a uniform resolution $\Delta x = \Delta y = \Delta = 0.002$. Magnetic field lines coincide with contours of A_z, and are thus plotted according to $A_z = 0.16i - 2$, with $i = 1, 2, \ldots, 24$.

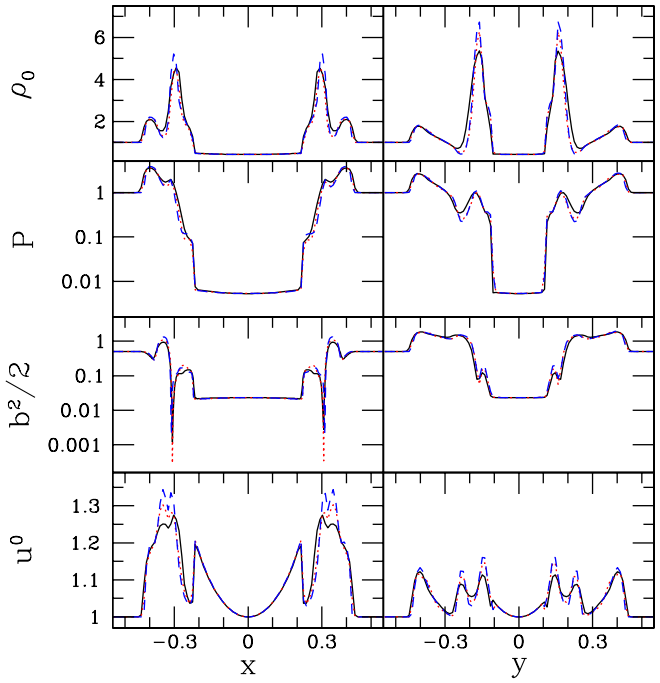

FIG. 9 (color online). Cylindrical rotating disk (rotor) test: 1D MHD variable profiles at different resolutions. Density ρ_0, pressure P, magnetic pressure $b^2/2$, and Lorentz factor u^0 along the x-axis (left) and y-axis (right) at $t = 0.4$ are plotted, at resolutions $\Delta = 0.004$ (black solid line), 0.0025 (red dotted line) and 0.002 (blue dashed line).

initial u^0 decreases from 10 at the edge of the disk to 4.5 at the next grid point inside the disk. While the three simulations produce the same qualitative result, proper convergence order is not likely to be achieved when this initial steep feature of the velocity is poorly resolved. However, we do find approximate second-order convergence in ρ_0 and b^2 in the region along the x-axis with $|x| < 0.2$ before the density, pressure and magnetic field display a sudden jump (see Fig. 9). On the other hand, u^0 and P converge faster than first order but less than second order in that region.

There are several conserved global quantities in two-dimensional Minkowski spacetime:

$$M = \iint \rho_0 u^0 dxdy = \sum_{i,j} \bar{\rho}_{*ij} \Delta x \Delta y, \tag{75}$$

$$E = \iint T^{00} dxdy = M + \sum_{i,j} \bar{\tilde{\tau}}_{ij} \Delta x \Delta y, \tag{76}$$

$$P_k = \iint T^0{}_k dxdy = \sum_{i,j} (\bar{\tilde{S}}_k)_{ij} \Delta x \Delta y, \tag{77}$$

$$J = \iint (xT^0{}_y - yT^0{}_x) dxdy, \tag{78}$$

where the sum is over all the grid points and the volume average is equivalent to the surface average over a grid cell in the x-y plane in two dimensions. Since there is no source term in Minkowski spacetime [i.e. $\boldsymbol{S} = 0$ in Eq. (33)], our finite-volume scheme should conserve M, E, and P_k to roundoff error, provided that no material flows through the boundary of the computation domain (i.e. $\boldsymbol{F} = 0$ at the outer boundary). This condition is satisfied in our rotor test, since the ambient medium is static and the torsional Alfvén wave generated by the rotor and the expansion of the high-density gas have not reached the boundary at the end of our simulations at $t = 0.4$. Our numerical data confirm that M, E and P_k are indeed conserved to roundoff error. On the other hand, the angular momentum will not be conserved to roundoff error since we use Cartesian coordinates to evolve the system. Strict numerical conservation of angular momentum can be achieved if cylindrical coordinates are adopted (however, P_x and P_y will not be strictly conserved in cylindrical coordinates). We find that for the rotor test at $t = 0.4$, J is changed by 1.7% from its initial value when evolved with resolution $\Delta = 0.004$, 1.2% with $\Delta = 0.0025$ and 1.0% with $\Delta = 0.002$. The slow decrease in J violation with resolution is again related to the insufficient resolution to resolve the initial steep u^0 profile near the edge of the rotor. We find that the numerically computed *initial* J deviates from the analytic value by 6.8%, 2.7% and 1.8% for $\Delta = 0.004$, 0.0025, and 0.002, respectively. This indicates that the thin layer near the edge of the rotor with high initial u^0 has a non-negligible contribution to J. Angular momentum conservation can be improved substantially if the thin layer is well-resolved.

It follows from the induction equation $\partial_t \boldsymbol{B} + \boldsymbol{\nabla} \times \boldsymbol{E} = 0$ that the global quantities

$$Q^k = \iint B^k dxdy \tag{79}$$

are conserved as long as $\boldsymbol{E}$ vanishes at the boundary. Since we do not evolve the volume-averaged B^i, but instead Eqs. (60)–(65), our scheme does not conserve Q^k to roundoff error. Instead, the quantities

$$Q^x_* = \sum_{ij} \langle B^x \rangle_{i+(1/2),j} \Delta x \Delta y \qquad Q^y_* = \sum_{ij} \langle B^y \rangle_{i,j+(1/2)} \Delta x \Delta y \tag{80}$$

are strictly conserved in our scheme. Our numerical data confirm this expectation. The deviation between Q^k and Q^k_* converges to zero at second order with increasing resolution. Unlike the angular momentum, the strict conservation of Q^k_* means that $Q^k - Q^k_*$ is time independent and therefore will not grow with time during the evolution.

B. Curved spacetime test: Relativistic Bondi flow

Next, we test the ability of our code to accurately evolve the relativistic MHD equations in a strongly curved spacetime near a black hole. We perform the magnetized

relativistic Bondi accretion test. Bondi accretion refers to spherically symmetric, steady-state accretion of a unmagnetized, adiabatic gas onto a stationary star. The gas is assumed to be homogeneous and at rest far from the star and flow adiabatically with a Γ-law EOS. Analytic solutions for Bondi accretion onto a Schwarzschild black hole are given in [53,54]. It has been shown that the relativistic Bondi solution is unchanged in the presence of a divergenceless radial magnetic field [55].

This test is a powerful one, since it combines strongly curved spacetime and relativistic flows with an analytic solution against which we compare our numerical results. It can also be used to test the ability of our AMR GRMHD scheme to handle the black hole interior, especially the coordinate singularity at the center. The use of refinement boxes is natural, since higher resolution is required in the vicinity of the black hole, whereas a relatively low resolution is sufficient to resolve the region far away from the black hole. In addition to simulations on a fixed-background spacetime, we also evolve the black hole spacetime using the puncture technique. The spatial metric then evolves from the puncture initial data to the trumpet solution [56,57]. Although this evolution is a pure gauge effect, the spatial metric and extrinsic curvature change with time, and the gas and magnetic field will respond to this change.

In general, a spherically symmetric spatial metric can be written in the form

$$^{(3)}ds^2 = \Lambda(r,t)dr^2 + \lambda(r,t)r^2(d\theta^2 + \sin^2\theta d\phi^2). \quad (81)$$

It is easy to show that any divergenceless, radial magnetic field is given by

$$B^r(r,t) = \frac{B_0 M^2}{\sqrt{\Lambda(r,t)}\lambda(r,t)r^2}, \quad (82)$$

where M is the mass of the black hole and B_0 is a constant characterizing the strength of the magnetic field. Cartesian coordinates can be constructed from the usual transformation: $x = r\sin\theta\cos\phi$, $y = r\sin\theta\sin\phi$ and $z = r\cos\theta$. The Cartesian components of the magnetic field B^i is given by

$$B^i(\boldsymbol{x},t) = \frac{B_0 M^2 x^i}{\sqrt{\gamma(\boldsymbol{x},t)}r^3}, \quad (83)$$

where the determinant γ of the spatial metric γ_{ij} in Cartesian coordinates is given by $\gamma(\boldsymbol{x},t) = \Lambda(r,t)\lambda^2(r,t)$. It is easy to show that this magnetic field can be derived from the vector potential

$$A_x = -\frac{B_0 M^2 y}{r(r+z)}, \qquad A_y = \frac{B_0 M^2 x}{r(r+z)}, \qquad A_z = 0. \quad (84)$$

We note that Eq. (83) is quite general. The radial coordinate r can be the Kerr-Schild radius, the shifted Kerr-Schild radius considered below, the isotropic radial coordinate in the puncture initial data, or the radial coordinate in the trumpet solution of a Schwarzschild black hole. During the puncture evolution of a Schwarzschild black hole, the radial coordinate $r = \sqrt{x^2 + y^2 + z^2}$ in the numerical simulation changes from the isotropic radial coordinate to the radial coordinate of the trumpet solution. Equation (83) will remain valid if the evolution preserves spherical symmetry.

The parameters of the magnetized Bondi test presented here are the same as those used by [55,58,59]. The sonic radius exists at Schwarzschild (areal) radius $r_s = 8M$. The density is normalized so that the mass accretion rate is $\dot{M} = 1$, and the equation of state is $\Gamma = 4/3$. The initial data for the hydrodynamic variables are given by the analytic solution, and the magnetic vector potential is given by Eq. (84). We parametrize the strength of the magnetic field by the ratio b^2/ρ_0 at the event horizon. The relationship between B_0 and $(b^2/\rho_0)_{\rm horizon}$ can be computed analytically and is given by

$$B_0 = \frac{2.2688}{M}\sqrt{\left(\frac{b^2}{\rho_0}\right)_{\rm horizon}} \quad (85)$$

for the hydrodynamic setup chosen here. We note that even though Eq. (85) is computed in Kerr-Schild radial coordinates, it applies to any other radial coordinate because B_0 is gauge-invariant. To see this, we compute b^2 at spatial infinity, where the gas is static. Using Eqs. (81), (82), and (10) we obtain

$$b^2(r) = \gamma_{rr}\frac{(B^r)^2}{4\pi} = \frac{B_0^2 M^4}{4\pi r_a^4} \quad \text{for } r \to \infty,$$

where $r_a = \sqrt{\lambda}r$ is the areal radius and we have used the fact that $\alpha u^0 = \sqrt{1 + \gamma^{ij}u_i u_j} = 1$ for a static ($u_i = 0$) gas. Hence we can write

$$B_0 = \lim_{r_a\to\infty} 4\pi\left(\frac{r_a}{M}\right)^4 b^2(r_a), \quad (86)$$

which is manifestly gauge-invariant.

In all of our simulations, we use five refinement boxes with half-side lengths of $3.125M$, $6.25M$, $12.5M$, $25M$, and $50M$. The outermost, lowest-resolution box possesses half-side length $100M$. We only evolve the space above and on the equatorial plane $z \geq 0$. Equatorial symmetry is applied to hydrodynamic variables and $(r+z)A_i$. All variables at the outer boundary are frozen to their initial values. Our standard resolution is $\Delta x = \Delta y = \Delta z = \Delta = 2.5M$ in the coarsest level. The grid spacing Δ decreases by a factor of 2 at each successive refinement level, so the resolution on the finest level is $\Delta_{\rm min} = M/12.8$. For the purposes of testing convergence, we also perform a simulation in which the resolution is scaled up so that $\Delta_{\rm min} = M/16$. To measure errors due to moving refinement boxes in our AMR scheme, we move refinement box centers according to

$$x_c = x_m\sin\omega t, \qquad y_c = y_m(1 - \cos\omega t), \quad (87)$$

where we set the parameters $x_m = 1.0M$, $y_m = 0.6M$ and $2\pi/\omega = 50M$. Below, we present results for the fixed-background spacetime simulations and the puncture evolution. Without loss of generality, we set $M = 1$ in all of our simulations.

1. Fixed-background spacetime

In many relativistic Bondi tests, Kerr-Schild coordinates are used together with excision. A different approach is adopted here. We first define a shifted Kerr-Schild radius $r = r_{\rm KS} - r_0$, where $r_{\rm KS}$ is the Kerr-Schild radius and r_0 is a constant chosen in the range $0 < r_0 < 2M$. We then construct Cartesian coordinates using the standard transformation between (x, y, z) and (r, θ, ϕ). The origin $x = y = z = 0$ therefore corresponds to a Kerr-Schild radius $r_{\rm KS} = r_0$. The region $r_{\rm KS} < r_0$ is excluded in this coordinate system and so is the black hole spacetime singularity. However, the origin is a coordinate singularity since the whole surface $r_{\rm KS} = r_0$ is mapped to a single point. This coordinate system thus mimics the trumpet solution of a Schwarzschild black hole. We set $r_0 = M$ for all the tests presented in this section. Just as in puncture evolutions, we do not use excision but shift the grid slightly so that the origin is not on a grid point.

We are able to evolve the system stably using the MC reconstruction scheme coupled with the HLL flux for $(b^2/\rho_0)_{\rm horizon} \lesssim 10$ with our standard resolution. Higher magnetic fields may be evolved if the resolution is increased. During the evolution, the magnetic field, as well as the density, increases linearly with time near the origin, creating jumps in the magnetic field that increase with time. This phenomenon causes the evolution near the origin to become more and more inaccurate. The inaccurate data spread out slowly from the origin to the apparent horizon, eventually crossing into the BH exterior. To overcome this difficulty, we add fourth-order Kreiss-Oliger dissipation to the evolved variables inside the horizon for radius $r < 0.8M$. We also set a density cap $\rho_0 < 1$ for radius $r < 0.5M$. This technique stabilizes the evolution near the origin and the system quickly settles down to a steady state inside the horizon. Figure 10 shows the profiles of ρ_0, v^x and B^x in the equatorial plane ($z = 0$) along the line $y = 0.01$ for $(b^2/\rho_0)_{\rm horizon} = 4$ at $t = 101.25M$, by which time the center of the refinement boxes has gone through slightly more than two rotations. The analytic solution and numerical data are plotted together for comparison. Vertical lines denote the location of the horizon $|x| = M$. We see that the profiles agree very well with the analytic solution outside the horizon. There are strong jumps in the magnitude and direction of the magnetic field near the coordinate singularity at the origin. The maximum and minimum values of B^x near the origin are 13.4 and -19.5 respectively, far outside the scale shown in the figure. However, these jumps are always contained near the coordinate singularity.

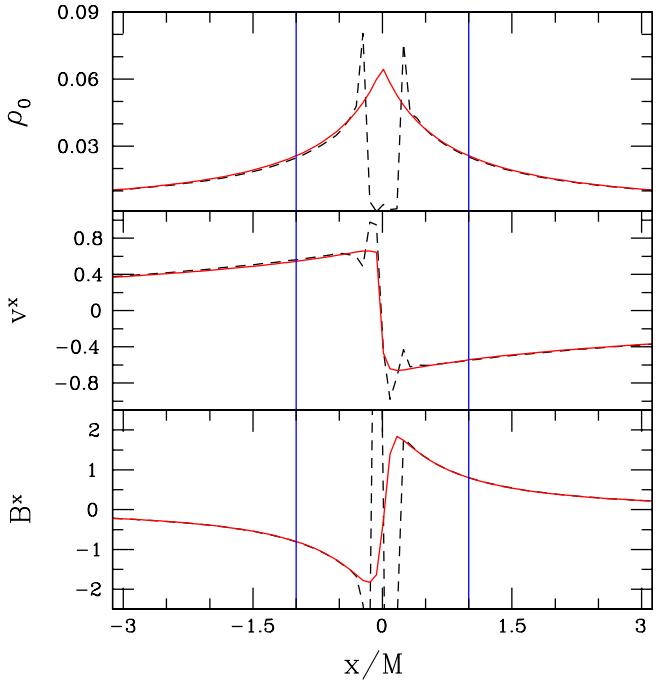

FIG. 10 (color online). Fixed-background, $(b^2/\rho_0)_{\rm horizon} = 4$ magnetized Bondi test: 1D MHD variable profiles. ρ_0, v^x and B^x are plotted in the equatorial plane ($z = 0$) along the line $y = 0.01M$ at $t = 101.25M$. Solid (red) lines are the analytic solution and dashed (black) lines are numerical data with $\Delta_{\rm min} = M/12.8$ on the finest refinement level, using MC reconstruction. The vertical lines denote the location of the event horizon $|x| = M$.

The evolution near the coordinate singularity at the origin is less stable when evolved with PPM reconstruction. To remedy this, we set $A_i = 0$ for radius $r < 0.5M$, well inside the horizon, in addition to the technique described above. Figure 11 shows profiles of MHD variables using PPM. We again see that the profiles agree well with the analytic solution outside the horizon, oblivious to the ruggedness of profiles in the black hole interior.

To check for convergence, we perform a number of simulations of varying $(b^2/\rho_0)_{\rm horizon}$ with two different resolutions $\Delta_{\rm min} = M/12.8$ and $\Delta_{\rm min} = M/16$. We compute the L2 norm of B^r at $t = 101.25M$ by summing over grid points

$$\mathrm{L}\,2(B^r) = \frac{\sum(B^r_{\rm numerical} - B^r_{\rm analytic})}{\sum B^r_{\rm analytic,1}}, \qquad (88)$$

where $B^r_{\rm analytic,1}$ denote the analytic values of B^r for $(b^2/\rho_0)_{\rm horizon} = 1$. We only computed the L2 norm in the innermost refinement level outside the horizon with $|x| < 3M$, $|y| < 3M$, $0 \le z < 3M$ and $r > M$. This is the region in the black hole exterior where the magnetic field is the strongest. Figure 12 shows the L2 norm as a function of $(b^2/\rho_0)_{\rm horizon}$. We see second-order convergence for $(b^2/\rho_0)_{\rm horizon} \lesssim 8$. The convergence rate appears to be

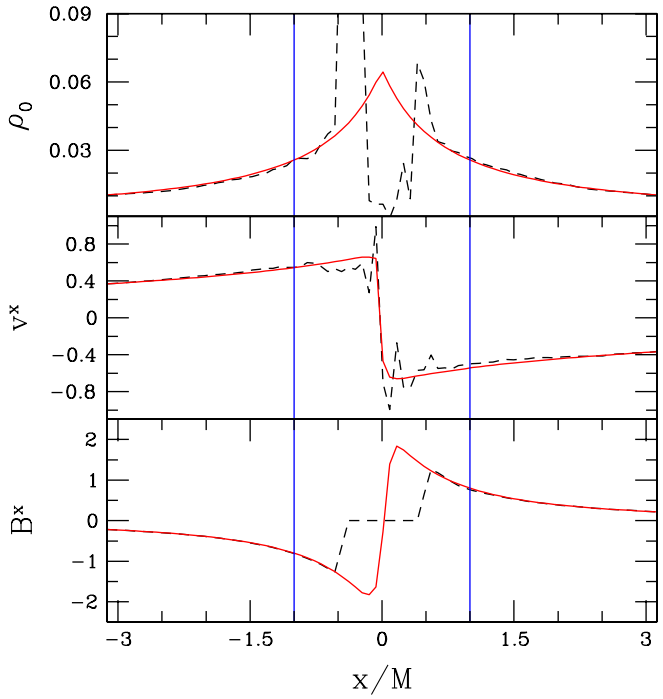

FIG. 11 (color online). Same as Fig. 10, but with PPM reconstruction for the numerical data, and setting $A_i = 0$ for deep inside the BH ($r < 0.5M$).

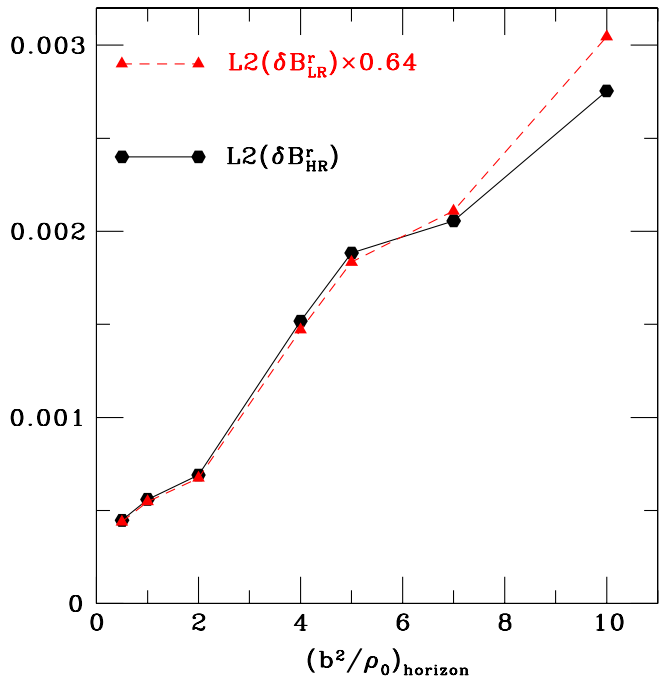

FIG. 12 (color online). Fixed-background magnetized Bondi test: Convergence study using MC reconstruction. L2 norm of B^r as a function of $(b^2/\rho_0)_{\text{horizon}}$ is plotted at $t = 101.25M$ for lower ($\Delta_{\min} = M/12.8$) and higher ($\Delta_{\min} = M/16$) resolution runs. The lower resolution result is multiplied by the factor 0.64 to demonstrate second-order convergence.

higher than second order for $(b^2/\rho_0)_{\text{horizon}} = 10$, indicating that the data in the lower resolution run may not be accurate enough to display proper convergence.

2. Puncture evolution

In addition to the evolution with a fixed-background metric, we perform several magnetized Bondi tests with a *time-dependent* background metric. We evolve the black hole spacetime using the puncture technique. In order to compare with the analytic solution, we set the matter and EM field source terms to zero in the BSSN equations, so that the gas and EM field do not affect the spacetime evolution, consistent with assumptions used when deriving the analytic solution. However, the gas and EM field will respond to the change of the background metric since the MHD and induction equations contain metric quantities. The metric evolution is a pure gauge effect: the spatial metric and extrinsic curvature evolve from the initial maximal, wormhole slicing to the final slicing representing the trumpet geometry.

We evolve the MHD and induction equations using both MC and PPM reconstruction, coupled with the HLL flux. A fourth-order Kreiss-Oliger dissipation is applied to the MHD evolution variables for $r < 0.5M$, which is inside the horizon at all times. As before, we set $A_i = 0$ for $r < 0.5M$ in the PPM run to stabilize the evolution near the puncture. Figure 13 shows the profile of B^x at $t = 101.25M$ in the equatorial plane ($z = 0$) along the line $y = 0.01M$ for $(b^2/\rho_0)_{\text{horizon}} = 4$. Numerical data are compared to Eq. (83) with $\sqrt{\gamma} = e^{6\phi}$ taken from the numerical data. We see that the data agree well with the analytic result outside the horizon in both runs. The glitch near the origin results from the loss of accuracy of ϕ near the puncture. When compared with Fig. 10, we see that the B^x profile is smooth in the puncture evolution with MC reconstruction. However, we find a similar feature in the ρ_0 profile as in Fig. 10.

Since the analytic solution of the hydrodynamic quantities are given in Kerr-Schild coordinates, direct comparison of numerical and analytic results is not easy in these simulations. However, since both b^2 and ρ_0 are scalar and the system is stationary, the profile of b^2 as a function of ρ_0 is gauge-independent. Figure 14 shows this function at $t = 101.25M$ in the equatorial plane along the line $y = 0.01$ and $x > 0.5M$ for two resolutions. The numerical profile of ρ_0 is no longer monotonically increasing with decreasing r when the numerical data inside the horizon are included, due to inaccuracy near the puncture. We therefore remove the data points inside the horizon for $x < x_0$ to prevent multiple values of $b^2(\rho_0)$ from appearing in the plot, where x_0 is the point when ρ_0 reaches the maximum. The position of the horizon is indicated by the vertical line $\rho_0 = (\rho_0)_{\text{horizon}} = 0.02579$, the value of ρ_0 at the horizon. The deviation between the numerical data and analytic result becomes visible close to the horizon in the lower resolution

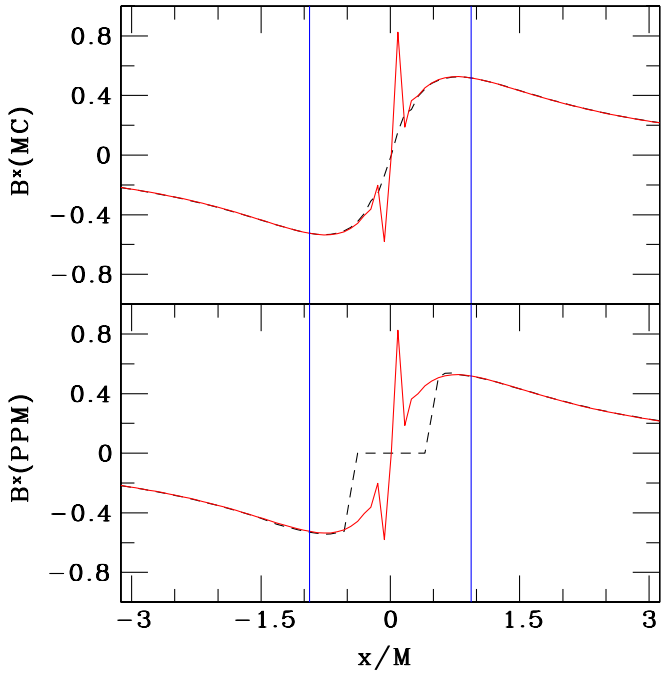

FIG. 13 (color online). Evolved-spacetime, $(b^2/\rho_0)_{\rm horizon} = 4$ magnetized Bondi test: Profile of B^x at $t = 101.25M$ in the equatorial plane ($z = 0$) along the line $y = 0.01M$. The metric is evolved using the puncture technique. The upper graph plots numerical data using MC reconstruction, and the lower graph shows the result using PPM reconstruction and setting $A_i = 0$ for $r < 0.5M$. Dashed (black) lines are numerical data, and solid (red) lines are results computed by Eq. (83) with $\sqrt{\gamma} = e^{6\phi}$ taken from numerical data. The glitch near $x = 0$ results from the loss of accuracy of the metric data close to the puncture. The vertical lines denote the location of the black hole horizon $|x| = 0.94M$.

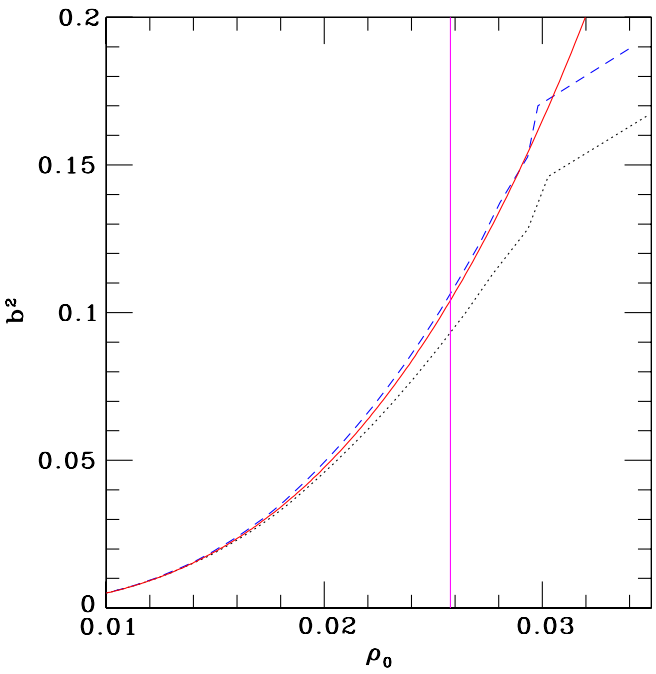

FIG. 14 (color online). Evolved-spacetime, $(b^2/\rho_0)_{\rm horizon} = 4$ magnetized Bondi test: Convergence of b^2 as a function of ρ_0 at $t = 101.25M$ along the line $x > 0.5M$, $(y, z) = (0, 0.01M)$. The background metric is evolved using the puncture technique. Dotted (black) and dashed (blue) lines plot the numerical data evolved with MC reconstruction using resolutions $\Delta_{\rm min} = M/12.8$ and $\Delta_{\rm min} = M/16$, respectively. The solid (red) line denotes the analytic profile, and the vertical line demarcates the horizon boundary, where $\rho_0 = (\rho_0)_{\rm horizon} = 0.02579$. The region with $\rho_0 > (\rho_0)_{\rm horizon}$ lies inside the horizon.

run $\Delta_{\rm min} = M/12.8$. Much better agreement is achieved in the higher resolution run with $\Delta_{\rm min} = M/16$. This is not surprising since $M/12.8$ is a fairly poor resolution for puncture simulations.

C. Curved spacetime test: Collapse of magnetized rotating relativistic star

This test focuses on magnetized, rotating, relativistic stellar-collapse simulations. The initial stellar configuration is the same as Star D in [60] and Star B in [1]. The star satisfies a $\Gamma = 2$ polytropic EOS and is uniformly rotating with $J/M^2 = 0.34$, where J is the angular momentum. The ADM mass of the star is $M = 1.04M_{\rm TOV}$, where $M_{\rm TOV}$ is the maximum ADM mass of a nonrotating relativistic star satisfying $\Gamma = 2$ EOS. The star is on the unstable branch of the constant J sequence, and previous numerical simulations have demonstrated that it is dynamically unstable to gravitational collapse [1,60].

In all of our simulations, we use seven refinement boxes with half-side lengths of $0.9143M$, $1.829M$, $3.657M$, $7.314M$, $14.63M$, $29.26M$ and $58.51M$. The box containing the outer boundary has half-length $117.0M$. The initial coordinate radius of the star in the equatorial plane is $3.485M$. Hence the stellar interior is initially covered by the three innermost refinement boxes. The grid spacing is reduced by a factor of 2 at each successive refinement level. We perform three simulations with the resolution in the finest refinement level set to $\Delta_{\rm min} = 0.02857M$ (low resolution run), $0.02287M$ (medium resolution run), and $0.01829M$ (high-resolution run).

We evolve the metric using a fourth-order finite-differencing scheme. We adopt the puncture gauge conditions with the shift parameter η set to $0.5/M$. The MHD and induction equations are evolved using the PPM reconstruction scheme coupled with the HLL flux. Equatorial symmetry is applied to all variables. We maintain a low-density atmosphere in the computational domain with $\rho_{\rm atm} = 10^{-10}\rho_{\rm max}(0)$ and $P_{\rm atm} = P_{\rm cold}(\rho_{\rm atm})$ as described in Sec. III E. The Sommerfeld outgoing wave boundary condition is applied to the BSSN evolution variables, and outflow boundary conditions are applied to the hydrodynamic primitive variables, while the vector potential A_i is linearly extrapolated to the boundary.

Since the star is unstable, collapse can be triggered by numerical truncation error during the evolution. However,

since the truncation error is reduced with increasing resolution, subsequent evolution of the star will depend sensitively on resolution, which is not desirable for a convergence test. We therefore induce the collapse by depleting the initial pressure by 1%. We set up a small, poloidal, axisymmetric magnetic field by setting the vector potential as follows:

$$A_x = -yA_b \max(P - P_{\rm cut}, 0), \tag{89}$$

$$A_y = xA_b \max(P - P_{\rm cut}, 0), \tag{90}$$

$$A_z = 0, \tag{91}$$

where $P_{\rm cut}$ is set to 4% of the initial maximum pressure. The constant parameter A_b determines the strength of the magnetic field. We characterize the strength of the magnetic field by the ratio of the magnetic energy $\mathcal{M}$ to the internal energy $E_{\rm int}$. These energies are defined as

$$E_{\rm int} = \int \sqrt{-g}(\rho_0 \epsilon) u^0 d^3x, \tag{92}$$

$$\mathcal{M} = \int \sqrt{-g}(b^2/2) u^0 d^3x. \tag{93}$$

We have chosen a magnetic field strength of $\mathcal{M}/E_{\rm int} = 7.3 \times 10^{-3}$, which introduces only a small perturbation to the star.

Figure 15 shows the evolution of the central lapse for the three resolution runs. As the star is collapsing, the lapse decreases and an apparent horizon appears at time $t \sim 70M$. The large energy density and magnetic pressure inside the horizon cause the code to crash soon after its formation. This difficulty can be overcome by evacuating the hydrodynamic matter and magnetic field deep inside the horizon soon after the formation of horizon. The evolution then proceeds stably, and the spacetime settles to a Kerr black hole after $t \gtrsim 75M$ (see Fig. 16), with virtually no fluid or magnetic fields left outside the horizon. The mass and spin of the black hole are computed using the isolated and dynamical horizon formalism [61], with the axial Killing vector field computed using the numerical technique described in [62]. We find $M_{\rm BH} \approx M$ and $J_{\rm BH} \approx J$ ($a_{\rm BH}/M_{\rm BH} = J/M^2 = 0.34$) for all three resolution runs once all the matter enters the horizon, where M and J are the initial ADM mass and angular momentum of the star, respectively. This is expected since the collapse is nearly axisymmetric, and only a negligible amount of mass as well as angular momentum is radiated by the gravitational waves. (Recall that no angular momentum is radiated in strict axisymmetry.)

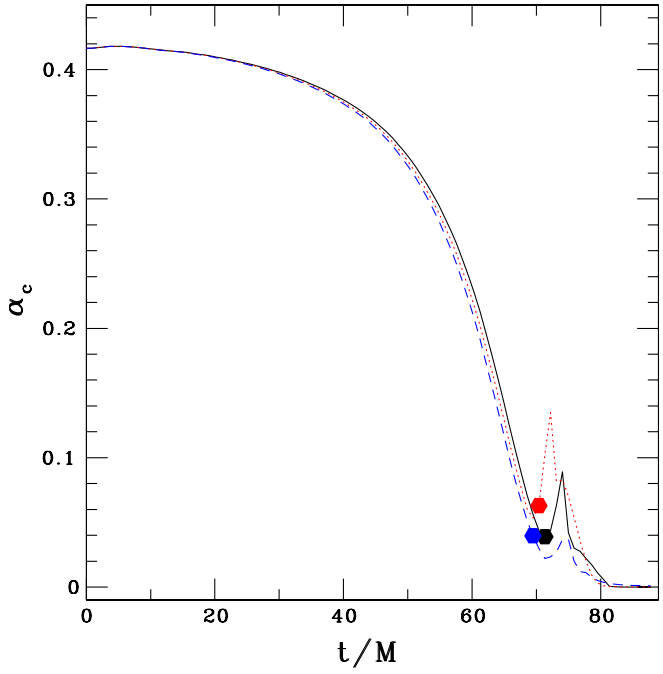

FIG. 15 (color online). Magnetized stellar collapse test: Evolution of the central lapse α_c for the low (black solid line), medium (red dotted line), and high (blue dashed line) resolution runs. The dot in each case indicates the time at which the apparent horizon appears. The increase in α_c soon after the horizon formation is caused by the loss of accuracy in metric evolution near the newly formed puncture, which is located near the coordinate origin and is deep inside the horizon.

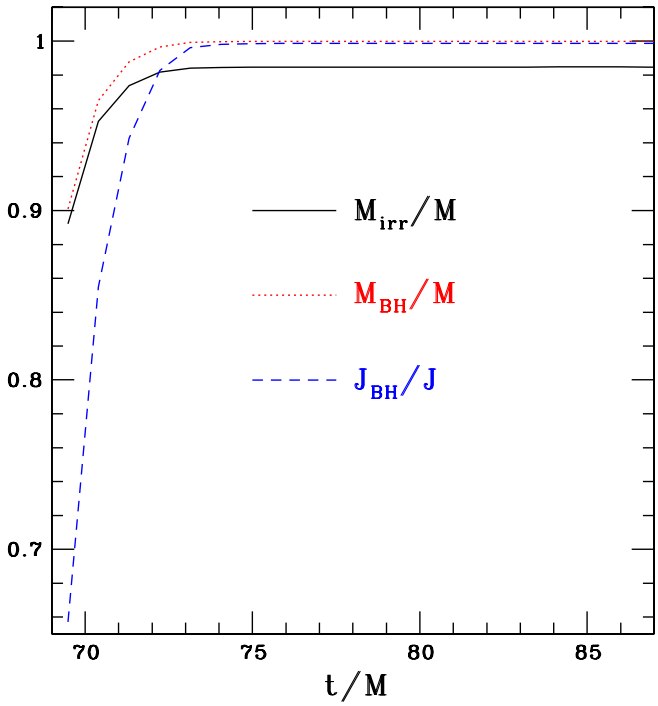

FIG. 16 (color online). Magnetized stellar collapse test: Evolution of the irreducible mass $M_{\rm irr}$, black hole mass $M_{\rm BH}$ and angular momentum $J_{\rm BH}$, as normalized by the initial ADM mass M and angular momentum J. Shown here are data from the high-resolution run. Results from the low- and medium-resolution runs are similar.

Figure 17 shows the profile of magnetic pressure $P_{\rm mag} = b^2/2$ along the diagonal line $x = y = z$ at $t = 40.2M$. We see slightly higher than second-order convergence in the high $P_{\rm mag}$ region but lower than second order in the low $P_{\rm mag}$ region.

In the simulation with the highest resolution, we find that the vector potential A_i develops spikes near the second innermost refinement boundary during and after the edge of the $A_i = 0$ surface passes through that refinement boundary. The amplitude of the spikes amplifies with time, eventually causing the code to crash. This difficulty can be removed by adding a fourth-order Kreiss-Oliger dissipation to A_i. The origin of the spikes is from prolongation and restriction. As A_i are steeply decreasing to zero near the edge, our adopted third-order Lagrangian interpolation scheme adds spurious oscillations in A_i near the refinement boundary after prolongation and restriction. Since the refinement boxes are not moving, the oscillation amplitude amplifies each time when prolongation and restriction are applied. The same phenomenon could occur for other hydrodynamical variables with a steep gradient.

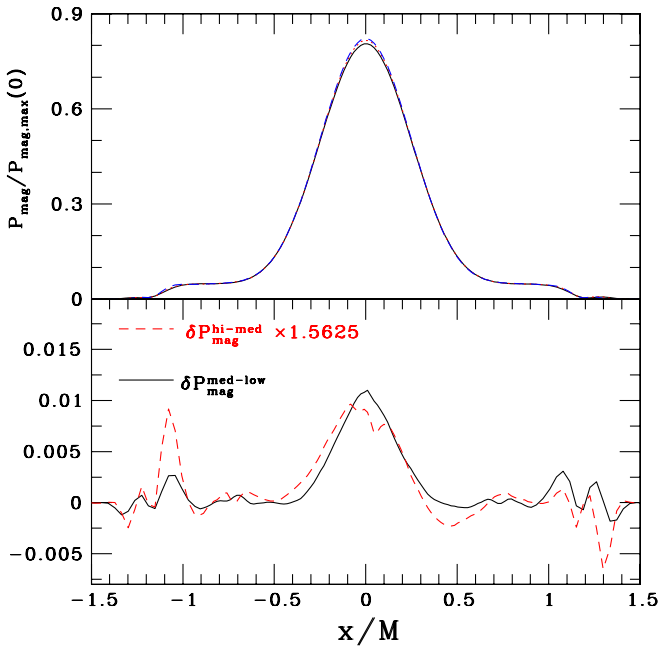

FIG. 17 (color online). Magnetized stellar collapse convergence tests. Upper graph: Magnetic pressure $P_{\rm mag} = b^2/2$ as a function of x along the diagonal line $x = y = z$ at time $t = 40.2M$ for the low (black solid line), medium (red dotted line) and high (blue dashed line) resolution runs, normalized by the initial maximum value of $P_{\rm mag}$. Lower graph: Pairwise differences of $P_{\rm mag}$ between different resolution runs. The difference $\delta P^{\rm hi-med}_{\rm mag} = (P^{\rm hi}_{\rm mag} - P^{\rm med}_{\rm mag})/P_{\rm mag,max}(0)$ is multiplied by 1.5625 to demonstrate deviations from second-order convergence. Notice that the results converge slightly higher than second order in the high $P_{\rm mag}$ region but less than second order in the low $P_{\rm mag}$ region.

However, this effect has a more significant impact on the magnetic field, since a slight spatial oscillation in A_i will be amplified after taking spatial derivatives. An alternative method to cure this problem would be to use a more sophisticated interpolation scheme such as the ENO or WENO scheme. We plan to investigate these alternative interpolation schemes in the future.

V. CONCLUSION

We have developed a new GRMHD code that is capable of evolving MHD fluids in dynamical spacetimes. We use the BSSN scheme coupled with the puncture gauge conditions to evolve the metric, and an HRSC scheme to evolve the MHD and induction equations.

We adopt the formalism described in [27] to recast the induction equation into an evolution equation for the magnetic vector potential A_i [i.e. Eq. (18)]. The variables A_i are stored on a staggered grid with respect to the other variables. The divergenceless constraint $\nabla \cdot \boldsymbol{B} = 0$ is imposed through the vector potential. This evolution scheme is AMR-compatible, with prolongation and restriction applied to the unconstrained variables A_i instead of B^i, which gives us flexibility in choosing different interpolation schemes for prolongation/restriction. In simulations with uniform grid spacing, our scheme for evolving the magnetic field is numerically equivalent to the commonly used constrained-transport scheme based on a staggered-mesh algorithm [16].

We have performed several code tests to validate our code, including magnetized shocks, nonlinear Alfvén waves, cylindrical blast explosions, cylindrical rotating disks, magnetized Bondi tests, and collapse of magnetized rotating stars. We find good agreement between the analytic and numerical solutions, and achieve second-order convergence for smooth flows, as expected.

In GRMHD simulations in dynamical spacetimes involving black holes, one delicate issue is the handling of the black hole interior. We adopt the moving puncture technique in which the black hole spacetime singularity is avoided by the puncture gauge conditions. However, a coordinate singularity (puncture) remains in the black hole interior, which could cause numerical difficulties in MHD simulations. In our tests involving black holes, we find that the evolution in the black hole interior is more stable when a more diffusive scheme such as the MC reconstruction scheme is used rather than the PPM scheme. We plan to investigate the idea of using a less diffusive scheme (such as PPM reconstruction coupled with the HLL flux) in the black hole exterior and a more diffusive scheme (such as MC or minmod reconstruction coupled with the LLF flux) in the black hole interior. A similar technique is used in some MHD simulations of magnetized accretion disks around a black hole [63]. We also find that adding Kreiss-Oliger dissipation to MHD variables in the black hole interior can stabilize the evolution.

In GRMHD simulations using an FMR grid, we find that applying a high-order interpolation scheme on A_i during prolongation and restriction could cause oscillations in A_i near the refinement boundaries. The oscillation amplitude can amplify with time. This numerical artifact degrades the accuracy of the simulation and could even cause the code to crash. The artifact can be removed by adding a fourth-order Kreiss-Oliger dissipation to A_i. A better solution is to use a more sophisticated interpolation scheme for A_i, such as the ENO or WENO scheme. We plan to investigate these alternative schemes in the future.

In addition to the treatment of the black hole interior, our MHD code has limitations similar to those of other MHD codes in the literature. In particular, accurate evolution is difficult when $b^2 \gg \rho_0$. This could potentially cause problems in the low-density regions in some applications. However, our experience and the experience of other numerical MHD groups suggests that these difficulties are surmountable.

Having demonstrated the validity of our AMR GRMHD code, we will next apply our code to study the effects of magnetic fields in the coalescence of binary neutron star and black-hole-neutron star systems, the collapse of magnetized supermassive stars, and the dynamics of magnetized accretion disks around merging binary black holes.

ACKNOWLEDGMENTS

This paper was supported in part by NSF Grants PHY06-50377 and PHY09-63136 as well as NASA NNX07AG96G and NNX10A1736 to the University of Illinois at Urbana-Champaign. Simulations were performed under a TeraGrid Grant TG-MCA99S008 and on the Illinois Numerical Relativity Beowulf Cluster.

[1] M. D. Duez, Y. T. Liu, S. L. Shapiro, and B. C. Stephens, Phys. Rev. D **72**, 024028 (2005).
[2] M. Shibata and T. Nakamura, Phys. Rev. D **52**, 5428 (1995).
[3] T. W. Baumgarte and S. L. Shapiro, Phys. Rev. D **59**, 024007 (1998).
[4] G. Tóth, J. Comput. Phys. **161**, 605 (2000).
[5] M. D. Duez, Y. T. Liu, S. L. Shapiro, M. Shibata, and B. C. Stephens, Phys. Rev. Lett. **96**, 031101 (2006).
[6] M. D. Duez, Y. T. Liu, S. L. Shapiro, M. Shibata, and B. C. Stephens, Phys. Rev. D **73**, 104015 (2006).
[7] B. C. Stephens, S. L. Shapiro, and Y. T. Liu, Phys. Rev. D **77**, 044001 (2008).
[8] M. Shibata, Y. T. Liu, S. L. Shapiro, and B. C. Stephens, Phys. Rev. D **74**, 104026 (2006).
[9] Y. T. Liu, S. L. Shapiro, and B. C. Stephens, Phys. Rev. D **76**, 084017 (2007).
[10] Y. T. Liu, S. L. Shapiro, Z. B. Etienne, and K. Taniguchi, Phys. Rev. D **78**, 024012 (2008).
[11] Z. B. Etienne, J. A. Faber, Y. T. Liu, S. L. Shapiro, K. Taniguchi, and T. W. Baumgarte, Phys. Rev. D **77**, 084002 (2008).
[12] Z. B. Etienne, Y. T. Liu, S. L. Shapiro, and T. W. Baumgarte, Phys. Rev. D **79**, 044024 (2009).
[13] B. D. Farris, Y. T. Liu, and S. L. Shapiro, Phys. Rev. D **81**, 084008 (2010).
[14] J. U. Brackbill and D. C. Barnes, J. Comput. Phys. **35**, 426 (1980).
[15] D. S. Balsara and D. S. Spicer, J. Comput. Phys. **149**, 270 (1999).
[16] C. R. Evans and J. F. Hawley, Astrophys. J. **332**, 659 (1988).
[17] A. Dedner, F. Kemm, D. Kröner, C. Munz, T. Schnitzer, and M. Wesenberg, J. Comput. Phys. **175**, 645 (2002).
[18] M. Anderson, E. W. Hirschmann, S. L. Liebling, and D. Neilsen, Classical Quantum Gravity **23**, 6503 (2006).
[19] M. Campanelli, C. O. Lousto, P. Marronetti, and Y. Zlochower, Phys. Rev. Lett. **96**, 111101 (2006).
[20] J. G. Baker, J. Centrella, D.-I. Choi, M. Koppitz, and J. van Meter, Phys. Rev. Lett. **96**, 111102 (2006).
[21] Z. B. Etienne, J. A. Faber, Y. T. Liu, S. L. Shapiro, and T. W. Baumgarte, Phys. Rev. D **76**, 101503 (2007).
[22] D. Brown, O. Sarbach, E. Schnetter, M. Tiglio, P. Diener, I. Hawke, and D. Pollney, Phys. Rev. D **76**, 081503 (2007).
[23] D. Brown, P. Diener, O. Sarbach, E. Schnetter, and M. Tiglio, Phys. Rev. D **79**, 044023 (2009).
[24] M. Cécere, L. Lehner, and O. Reula, Comput. Phys. Commun. **179**, 545 (2008).
[25] D. S. Balsara, J. Comput. Phys. **174**, 614 (2001).
[26] D. S. Balsara, J. Comput. Phys. **228**, 5040 (2009).
[27] L. Del Zanna, N. Bucciantini, and P. Londrillo, Astron. Astrophys. **400**, 397 (2003).
[28] B. Brügmann, J. A. González, M. Hannam, S. Husa, U. Sperhake, and W. Tichy, Phys. Rev. D **77**, 024027 (2008).
[29] P. Marronetti, W. Tichy, B. Brügmann, J. González, and U. Sperhake, Phys. Rev. D **77**, 064010 (2008).
[30] C. O. Lousto and Y. Zlochower, Phys. Rev. D **79**, 064018 (2009).
[31] J. G. Baker, J. Centrella, D.-I. Choi, M. Koppitz, and J. van Meter, Phys. Rev. D **73**, 104002 (2006).
[32] L. Baiotti, B. Giacomazzo, and L. Rezzolla, Phys. Rev. D **78**, 084033 (2008).
[33] J. R. van Meter, J. G. Baker, M. Koppitz, and D.-I. Choi, Phys. Rev. D **73**, 124011 (2006).
[34] T. W. Baumgarte and S. L. Shapiro, Astrophys. J. **585**, 921 (2003).
[35] H. Janka, T. Zwerger, and R. Moenchmeyer, Astron. Astrophys. **268**, 360 (1993).
[36] http://www.cactuscode.org/.
[37] E. Schnetter, S. H. Hawley, and I. Hawke, Classical Quantum Gravity **21**, 1465 (2004).

[38] A. Harten and S. Osher, SIAM J. Numer. Anal. **24**, 279 (1987).
[39] X. Liu, S. Osher, and T. Chan, J. Comput. Phys. **115**, 200 (1994).
[40] G. Jiang and C. Shu, J. Comput. Phys. **126**, 202 (1996).
[41] Y. T. Liu, Z. B. Etienne, and S. L. Shapiro, Phys. Rev. D **80**, 121503 (2009).
[42] P. Colella and P. R. Woodward, J. Comput. Phys. **54**, 174 (1984).
[43] B. van Leer, J. Comput. Phys. **23**, 276 (1977).
[44] A. Harten, P. D. Lax, and B. J. van Leer, SIAM Rev. **25**, 35 (1983).
[45] S. C. Noble, C. F. Gammie, J. C. McKinney, and L. Del Zanna, Astrophys. J. **641**, 626 (2006).
[46] T. Yamamoto, M. Shibata, and K. Taniguchi, Phys. Rev. D **78**, 064054 (2008).
[47] M. Shibata, K. Kyutoku, T. Yamamoto, and K. Taniguchi, Phys. Rev. D **79**, 044030 (2009).
[48] T. Bode, R. Haas, T. Bogdanović, P. Laguna, and D. Shoemaker, Astrophys. J. **715**, 1117 (2010).
[49] J. A. Font, M. Miller, W. Suen, and M. Tobias, Phys. Rev. D **61**, 044011 (2000).
[50] S. S. Komissarov, Mon. Not. R. Astron. Soc. **303**, 343 (1999).
[51] S. S. Komissarov, Phys. Lett. A **232**, 435 (1997).
[52] M. Shibata and Y. Sekiguchi, Phys. Rev. D **72**, 044014 (2005).
[53] F. C. Michel, Astrophys. Space Sci. **15**, 153 (1972).
[54] S. L. Shapiro and S. A. Teukolsky, *Black Holes, White Dwarfs, and Neutron Stars: The Physics of Compact Objects* (Wiley, New York, 1983).
[55] J. De Villiers and J. F. Hawley, Astrophys. J. **589**, 458 (2003).
[56] M. Hannam, S. Husa, D. Pollney, B. Brügmann, and N. ÓMurchadha, Phys. Rev. Lett. **99**, 241102 (2007).
[57] M. Hannam, S. Husa, F. Ohme, B. Brügmann, and N. ÓMurchadha, Phys. Rev. D **78**, 064020 (2008).
[58] J. F. Hawley, L. L. Smarr, and J. R. Wilson, Astrophys. J. Suppl. Ser. **55**, 211 (1984).
[59] C. F. Gammie, J. C. McKinney, and G. Tóth, Astrophys. J. **589**, 444 (2003).
[60] M. D. Duez, P. Marronetti, S. L. Shapiro, and T. W. Baumgarte, Phys. Rev. D **67**, 024004 (2003).
[61] A. Ashtekar and B. Krishnan, Living Rev. Relativity **7**, 10 (2004).
[62] O. Dreyer, B. Krishnan, D. Shoemaker, and E. Schnetter, Phys. Rev. D **67**, 024018 (2003).
[63] C. Gammie (private communication).